AGU PUBLICATIONS

JGR

Journal of Geophysical Research: Oceans

RESEARCH ARTICLE

10.1002/2014JC009820

Key Points:
- Two-distinct regions of enhanced mesoscale activity to the south of Madagascar
- Southwest (southeast) region dominated by baroclinic (barotropic) instability
- Eddies have potential to trap and transport material from Madagascar to Africa

Correspondence to:
I. Halo,
issufo.halo@uct.ac.za

Citation:
Halo, I., P. Penven, B. Backeberg, I. Ansorge, F. Shillington, and R. Roman (2014), Mesoscale eddy variability in the southern extension of the East Madagascar Current: Seasonal cycle, energy conversion terms, and eddy mean properties, *J. Geophys. Res. Oceans*, *119*, 7324–7356, doi:10.1002/2014JC009820.

Received 16 JAN 2014
Accepted 10 SEP 2014
Accepted article online 18 SEP 2014
Published online 30 OCT 2014

Mesoscale eddy variability in the southern extension of the East Madagascar Current: Seasonal cycle, energy conversion terms, and eddy mean properties

Issufo Halo[1,2], Pierrick Penven[3], Björn Backeberg[1,2,4], Isabelle Ansorge[2], Frank Shillington[1,2], and Raymond Roman[2]

[1]Nansen-Tutu Centre for Marine Environmental Research, University of Cape Town, Cape Town, South Africa, [2]Department of Oceanography, MA-RE, University of Cape Town, Cape Town, South Africa, [3]LMI ICEMASA, Laboratoire de Physique des Océans, Ifremer, UMR 6523, CNRS/IFREMER/IRD/UBO, Plouzané, France, [4]Nansen Environmental and Remote Sensing Centre, Bergen, Norway

Abstract In this study, we used more than 17 years of satellite altimetry observations and output from an ocean model to investigate the mesoscale eddy variability and forcing mechanisms to the south of Madagascar. Analysis of energy conversion terms in the model has shown seasonality on eddy formation, both by barotropic and baroclinic instabilities: maximum in winter (JJA) and minimum in summer (DJF). The eddies were mainly formed in the upper ocean (0–300 m) and at intermediate depths (800–2000 m) by barotropic and baroclinic instabilities, respectively. The former dominated in the southeastern margin of Madagascar, and the latter to the southwest, where the South-East Madagascar Current (SEMC) separates from the continental shelf. Seasonality of the eddy formation appeared linked with the seasonal intensification of the SEMC. The energy conversion terms indicated that the eddies have a significant contribution to the large-scale circulation, but not being persistent throughout the year, occurring mainly during the fall season (MAM). Eddy demography from altimetry and model provided information on eddy preferential sites for birth, annual occurrence (6–13 per year), eddy mean diameter (124–178 km), mean amplitude (9–28 cm), life-time (90–183 days), and maximum traveling distances (325–1052 km). Eddies formed to the southwest of Madagascar exhibited distinct characteristics from those formed in the southeast. Nevertheless, all eddies were highly nonlinear, suggesting that they are potential vectors of connectivity between Madagascar and Africa. This may have a significant impact on the ecology of this region.

1. Introduction

The present description of the circulation in the southwest Indian Ocean, to the south of the Mozambique Channel and the Madagascar Island is that sketched in Figure 1a. It involves two poleward western boundary flows, the Agulhas Current (AC) at the southeast coast of South Africa, transporting ~70 Sv (1Sv = 10^6 m s^{-3}) in the upper 2000 m depth [*Donohue et al.*, 2000; *Lutjeharms*, 2006], and the South-East Madagascar Current (SEMC) at the southeast coast of Madagascar, carrying variable quantities ~22 Sv in the upper 1500 m depth [*Schott et al.*, 1988; *Schott and McCreary*, 2001], or larger ~32–37 Sv [*Nauw et al.*, 2008]. The SEMC is a narrow current (width ~120 km) with typical velocities of ~1.1 m s^{-1} [*Nauw et al.*, 2008], and derives its waters from the westward South Equatorial Current (SEC) that splits between 17°S and 20°S at the east coast of Madagascar [*Lutjeharms et al.*, 1981, 2000; *Chapman et al.*, 2003]. Direct observations of the velocity field from a ship-mounted and lowered ADCP across four hydrographic sections perpendicular to the SEMC, revealed the presence of an equatorward East Madagascar Undercurrent (EMUC), carrying ~2.8 Sv [*Nauw et al.*, 2008]. This undercurrent propagates at intermediate depths below the SEMC, and its core is centered between 1100 and 1800 m depth [*Nauw et al.*, 2008]. Another large-scale oceanographic feature present in the region is the shallow northeastward South Indian Ocean Countercurrent (SICC) [*Siedler et al.*, 2006; *Palastanga et al.*, 2007]. It is located offshore of the SEMC, and transports ~10 Sv in the upper 800 m depth [*Siedler et al.*, 2006] above SEC, along the 25°S latitude band [*Palastanga et al.*, 2007].

The AC and SEMC are separated by the Mozambique Basin (Figure 1a), and this region is characterized by intense mesoscale activity (Figure 1b). Large cyclonic and anticyclonic eddies [*Lutjeharms*, 1988;

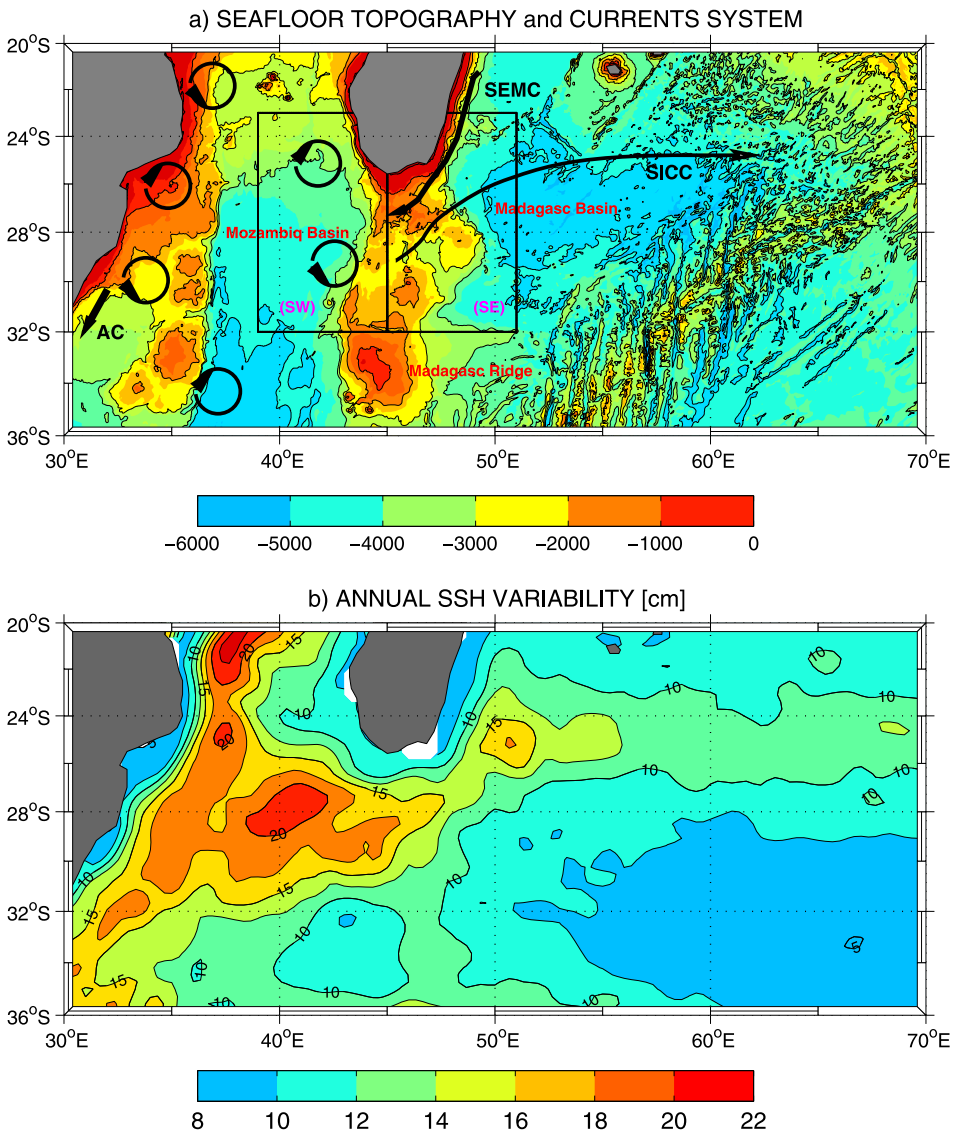

Figure 1. (a) Schematic of the circulation, superimposed on GEBCO1 topography with 1000 m contour intervals. South-East Madagascar Current (SEMC), South Indian Ocean Countercurrent (SICC), and Agulhas Current (AC). Clockwise (anticlockwise) features represent cyclonic (anticyclonic) eddies. (b) Sea surface ocean variability computed as root mean square (RMS) of the sea surface height derived from satellite altimetry, for the period starting from 14 October 1992 to 31 March 2010. The boxes in Figure 1a indicate southeast (SE) and southwest (SW) regions.

Gründlingh, 1995; *Lutjeharms et al*., 2000; *Quartly and Srokosz*, 2002], either isolated or paired as dipole structures [*de Ruijter et al*., 2004], propagate from the southeast of Madagascar toward the African continent. These eddies combined with the Mozambique Channel eddies and rings [*Biastoch and Krauss*, 1999; *de Ruijter et al*., 2002; *Schouten et al*., 2003; *Ridderinkhof and de Ruijter*, 2003; *Halo et al*., 2014] are important sources of the flow and variability for the AC [*van Leeuwen et al*., 2000; *Schouten et al*., 2002a, 2002b; *de Ruijter et al*., 2004].

For the marine ecosystems, the dynamics of the eddies in the southwest Indian Ocean have been described as the main mechanisms responsible for the variability of biological properties, such as nutrients and chlorophyll-a (indicative of phytoplankton community) [*Quartly and Srokosz*, 2004; *Tew-Kai and Marsac*, 2009; *Omta et al*., 2009; *Roshin et al*., 2010; *Srokosz and Quartly*, 2013]. Through surface divergence, eddies can upwell deep nutrient-rich waters important for the biological primary productivity [*Robinson*, 1983; *McGillicuddy et al*., 2007; *Chelton et al*., 2011a; *Lathuilière et al*., 2011]. Ocean eddies can also trap and

transport organic and inorganic materials over long distances [*Robinson*, 1983; *Provenzale*, 1999; *Thorpe*, 2007; *Chelton et al*., 2011b]. In line with these facts, it is thought that the eddies generated in the SEMC are potential vectors of connectivity of the marine fauna between Madagascar and KwaZulu-Natal, east coast of South Africa (*M. Roberts*, 2013, personal communication). A scientific research project termed "SuitCase" is ongoing with the aims to investigate the ecological linkages between the southeast of Madagascar and the east coast of South Africa (http://www.seaworld.org.za/research/entry/the-suitcase-project-eddies-as-potential-vectors-of-connectivity-between-ma). In this study, we provide corroborative evidence based on long-term satellite altimetric observation and model output that suggests such connectivity occurs, especially by the cyclonic eddy features.

Due to the paucity of in situ data, and an intense eddy field, the description of the circulation in this region is very complex, poorly understood, and to-date remains a subject of different interpretations: some arguing that the termination of the SEMC is a straight throughflow, as a main tributary to the Agulhas Current proper [*Gründlingh*, 1985; *Tomczak and Godfrey*, 1994; *Quartly and Srokosz*, 2004], while others suggest that it retroflects [*Lutjeharms and Roberts*, 1988; *Lutjeharms*, 1988; *Quartly et al*., 2006]. Later analysis of altimetry data and model output by *Siedler et al*. [2009], inferred that the flow pattern is composed by two main regimes: in one regime the SEMC flows mostly westward, closer to the southern Madagascar continental slope, where it originates a cyclonic recirculation, with cyclonic eddies being formed at the inshore edge of the flow. On the other hand, the second regime is characterized by the SEMC at the south of the Island propagating mostly south-westward direction, away from the Madagascar slope, and sheds an anticyclonic loop recirculation, which favors a retroflection of the SEMC. However, a more recent work suggests that none of these regimes are supported by hydrographic data, and neither retroflection of the SEMC nor contribution of the SEMC toward the SICC occurs [*Ridderinkhof et al*., 2013]. Here on the basis of model output, we infer that there is a significant contribution of the SEC toward SICC, induced by mesoscale eddy activity but not sustained throughout the year.

While some studies have provided important information about the characteristics of the eddies formed in this region, such as mean size, amplitude, propagation speed [*de Ruijter et al*., 2004; *Quartly et al*., 2006; *Siedler et al*., 2009], yet detailed information in connection with their demographic properties at different scales is missing. Identification and tracking of eddies to study their demography is a complex process. *Quartly and Srokosz* [2002] used an automatic eddy detection method based on identification of SST anomalies greater than 0.4°C for anticyclones and smaller than -0.4° for cyclones, within a 200 km box. The method can be sensitive to the threshold value of the SST anomaly. It can lose accuracy in the case of weak SST gradients. *Quartly et al*. [2006] used a second algorithm, based on the work of *Isern-Fontanet et al*. [2006]. This method is also sensitive to the choice of the threshold value for the vorticity field. *de Ruijter et al*. [2004] have used an empirical approach to follow in time and space eddies by visually identifying surface field of sea level anomalies from satellite altimetry (1995–2000). Their statistics of the dipole structures have shown that about four eddies per year were generated in the south of Madagascar: the eddies radii ranged from 50 to 200 km, both cyclones and anticyclones, and their amplitudes span from 0.21 to 0.48 cm, and propagation speeds varied between 5 and 10 cm s^{-1}. A manual eddy tracking can be sensitive to human subjectivity. Therefore, in this study we apply a robust automatic algorithm to assess more accurately detailed eddy characteristics.

While two-distinct modes of variability differentiates the southeast from the southwest region of Madagascar [*Matano et al*., 1999], little is known about property difference in eddy characteristics between these two regions. Therefore, in combination with altimetry observations, output from an eddy simulating regional ocean model is used to investigate such property difference. Furthermore, in situ data used here provide basic estimates of two cyclonic eddy structures on either sides of the southern Madagascar shelf, and the characteristics of the SEMC at 25°S. Thus, this study provides complementary information that enhances the present knowledge of eddy variability in this region. This is granted by both a longer altimetry time series (∼20 year record) and improved skills of the algorithms to identify and track eddies [*Chelton et al*., 2011b; *Halo et al*., 2014].

This paper is structured as follows: section 2 describes the observations and model used. Section 3 presents the validation of the model. Section 4 assesses the mechanisms of eddy formation and section 5 describes the eddy tracking algorithm. The results and discussion are presented in section 6. The main findings are summarized in section 7.

2. Model and Observational Data

In combination with altimetry and in situ data, we used the CNES-CLS09 product, and drifter data to validate the model field.

2.1. Altimetry Data

To make an assessment of the observed eddy variability and properties, we used gridded maps of absolute dynamic topography, which combines sea level anomaly observations merged from satellites Jason-1, Envisat, GFO, ERS-1, ERS-2, and Topex/Poseidon with the CNES-CLS09 mean dynamic topography (MDT). The altimetry data used here spans from 14 October 1992 to 31 March 2010. The product is globally gridded at 1/4° × 1/4°, every 7 days [*Ducet et al*., 2000], produced by Ssalto/Duacs and distributed globally by AVISO, with support from CNES. The data set is suitable to study the mesoscale ocean variability in the region south of Madagascar, where the first internal Rossby radius of deformation ranges from 60 km in the north to 40 km in the south [*Chelton et al*., 1998].

2.2. CNES-CLS09 Data

To evaluate the model ocean current fields, we used the CNES-CLS09 data set [*Rio et al*., 2011], which represents surface geostrophic mean circulation. The data set is a global estimation of MDT, gridded at 1/4° × 1/4°, computed from combination of the Gravity Recovery and Climate Experiment mission (GRACE), altimetric measurements, and oceanographic in situ data from 1993 to 2008, which includes all hydrographic profiles from Argo floats array [*Rio et al*., 2011]. The product is known to resolve stronger gradients in western boundary currents, being in better agreement with independent in situ observations, than other MDT estimates [*Rio et al*., 2011]. The data set is distributed by the French CNES-CLS.

2.3. Hydrographic Data From the ASCLME Cruise

To evaluate the model eddy vertical structure, we used in situ data from the first multidiscipline cruise of the Agulhas Somali Current Large Marine Ecosystem (ASCLME) project, carried out in August and September 2008, on board of the r/v Fridtjof Nansen [*Krakstad et al*., 2008]. The vessel was equipped with a ship-mounted RD instruments 150 kHz ADCP which was used to obtain vertical profiles of current speed and direction in the upper layer (∼300 m), and a Seabird 911plus CTD plus to obtain vertical profiles of temperature, salinity, and oxygen at a maximum cast depth of 3000 m. The ADCP data used were 20 min ensembles with a depth bin length of 4 m. Navigation was provided by a Seapath DGPS system. Relating ADCP currents to geostrophic velocities is somewhat complicated as ADCP currents include ageostrophic flows such as drift currents, tides, and internal waves or inertial oscillations. *Donohue and Toole* [2003] showed tidal influences of around 5 cm/s in southeast of Madagascar and in the Mozambique Channel. To remove barotropic tidal component, we used the tidal estimate provided by the OSU inverse tidal model, TPX08-atlas (http:volkov.oce.orst.edu/tides/tpxo8_atlas.html). Here we only used data collected in two transects because they intersected important oceanographic features of interest in this study: a cyclonic eddy at 25°30S on the southwest coast of Madagascar, and a cyclonic eddy interacting with the SEMC at 25°S on the southeast coast.

2.4. Drifter Data

In combination with satellite altimetry to validate the model derived mesoscale activity, we also used quality-controlled velocity fields from satellite tracked surface drifting buoys [*Niiler et al*., 1995; *Hansen and Poulain*, 1996], from the Global Drifters Program. The drifters are drogued at 15 m depth following the mixed-layer currents [*Lumpkin and Flament*, 2007]. The velocity fields are derived at 6 hourly intervals using a 12 h centered differences of the interpolated positions [*Lumpkin and Flament*, 2013]. The data are known to allow a better spatial resolution of seasonal variations and ocean current fields [*Lumpkin and Flament*, 2013]. The drifter measurements used here span from 1992 to 2012. During this period, a total of 215 drifters entered in the region of study (20°E–70°E and 20°S–36°S), and were reinterpolated daily on a 1/2° × 1/2° grid.

2.5. ROMS Model

Model output provides a regular spatial and temporal sampling of the variables throughout the ocean column at a desirable resolution, thus it allows for a more detailed study of eddies [*Kurian et al*., 2011; *Chelton et al*., 2011b]. Because of few in situ observations available in the region and limitation of satellite altimetry

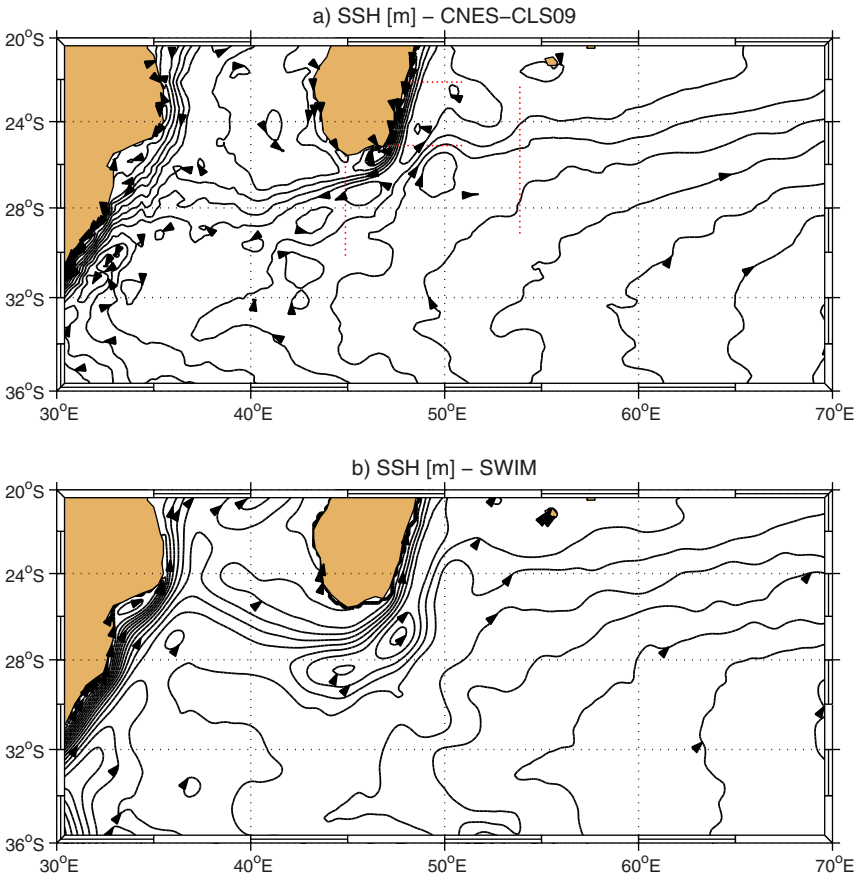

Figure 2. Streamlines of sea surface height (SSH) representing geostrophic mean circulation. (a) Mean dynamic topography (MDT) produced by CNES-CLS09, and (b) SWIM model 7 year climatology. The contours interval is 0.05 m, and the arrows indicate the direction of the flow. The transects are the positions used to calculate the volume transports of the SEMC at 22°S and at 54°E, and the vertical structures of the SEMC at 25°S and 45°E, and SICC at 54°E, presented in Figure 3.

data only at sea surface, we used also model derived data to give insight on the mechanisms of eddy formation in the water column. In fact, the assessment of eddy forcing mechanisms through energy transfer requires a vertical integration of the flow field components [*Marchesiello et al*., 2003]. Therefore, here we used the output from the South-West Indian Ocean Model (SWIM) configuration, which has been shown to provide a good representation of the main oceanographic features (hydrographic properties, mean circulation, the seasonal cycle, and the eddy variability) in the Mozambique Channel [*Halo et al*., 2014], and in the southwest Indian Ocean as a whole [*Halo*, 2012]. SWIM is based on the Regional Ocean Modelling Systems (ROMS) [*Shchepetkin and McWilliams*, 2005], and the configuration domain extends from 0°E to 77.5°E, and from 3°S to 47.5°S. It is forced at the surface by 1/2° × 1/2° gridded climatological fields from COADS05 [*da Silva et al*., 1994], and at the lateral boundaries by 1° × 1° gridded climatology from WOA05 [*Conkright et al*., 2002]. At the bottom, it uses the higher resolution topography from General Bathymetric Chart of the Oceans GEBCO1 [*Carpine-Lancre et al*., 2003]. The configuration runs at 1/5° horizontal grid resolution, with 45-vertical sigma-layers, for 10 years. It has been spun-up for 3 years and the output is averaged at 2 day time steps. In this study, the ability of the model to reproduce the oceanographic features of the region south of Madagascar is further demonstrated in the next section. However, a detailed description and validation of SWIM is presented by *Halo* [2012].

3. Model Validation

The ability of the model to reproduce the observed regional oceanographic features of the circulation is evaluated against formerly described observational data. Some published materials, such as that by *Donohue and Toole* [2003], *Siedler et al*. [2006], and *Nauw et al*. [2008] have been also used.

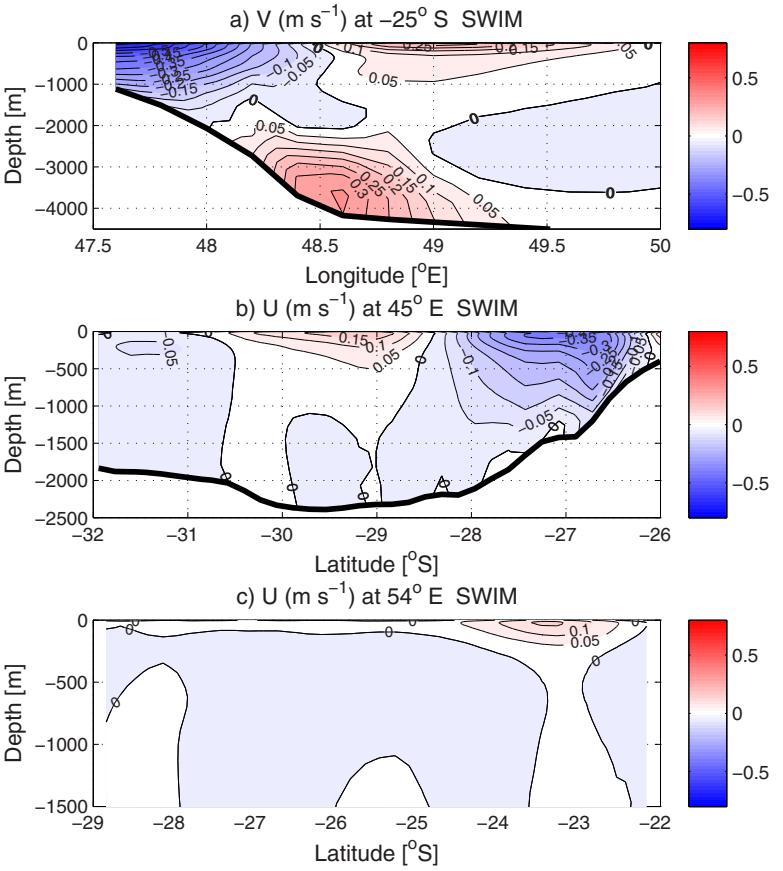

Figure 3. Vertical structures of the mean currents derived from SWIM model, 7 year climatology: (a) SEMC at 25°S, (b) both SEMC and SICC at 45°E, and (c) SICC at 54°E. Notice that section Figure 3a also captures an equatorward bottom boundary current below SEMC, and SICC offshore of SEMC. One may find more informative to compare Figures 3a and 3b against *Nauw et al*. [2008], their Figure 3, T8 and T5, respectively, and (c) against *Siedler et al*. [2006], their Figure 2a.

3.1. Surface Geostrophic Mean Circulation

Figure 2 shows streamlines of SSH (with 0.05 m contours interval) used as proxy for geostrophic mean ocean circulation. Figure 2a was derived from CNES-CLS09 data set and Figure 2b from the SWIM model, with stream arrows indicating the direction of flow. Similarities on the patterns of the streamlines in the model and observation are an indicative of convergency of results, which suggests that the model is reasonably accurate. Similar features to be noticed (one may find more informative to compare it with Figure 1a) are: the presence of the SEMC at the southeast coast of Madagascar; and offshore of the SEMC the presence of the SICC flowing northeastward between 28°S and 24°S, which is consistent with results from *Siedler et al*. [2006] and *Palastanga et al*. [2007]. On reaching the southern tip of Madagascar, it is evident patterns of cyclonic recirculation inshore and anticyclonic recirculation offshore of the SEMC, which is in agreement with hydrographic observations by *de Ruijter et al*. [2004]. It is also evident that the flow from the South of Madagascar and the Mozambique Channel is sources of the Agulhas Current, furthering agreeing with the studies by *Stramma and Lutjeharms* [1997] and *Lutjeharms* [2006]. However, some differences between the model and observations are obvious, especially directly south of Madagascar, at the offshore edge of the SEMC, where the model (Figure 2b) shows stronger anticyclonic recirculation which appears to suggest a retroflection of the SEMC, that feeds the SICC as proposed by *Siedler et al*. [2009]. Note also that the model appears to reproduce a relatively weaker SEMC, and a stronger boundary flow at the African continent, between 28°S and 24°S (Figure 2b). The reason for such behavior is not clear. However, one has to bear in mind that the CNES-CLS09 product is known to reproduce stronger gradients of western boundary mean flows [*Rio et al*., 2011]. Stronger gradients produced by the model between 28°S and 24°S could be associated to localized intense eddy activity (evident at the Delagoa Bight), which impacts the averaged field by producing a northward offshore component mostly depicted in Figure 2b.

3.2. Vertical Structure of the SEMC and SICC

Figure 3 shows model derived vertical structures of the mean currents system dominating the circulation in the region. Figure 3a was computed along 25°S, between 47.5°E and 50°E, across the meridional extension of the SEMC (see Figure 2a for reference). Its top left corner shows the SEMC clinging to the southern Madagascar continental slope. It penetrates ∼1800 m deep, and extends zonally offshore toward 48.5°E (being slightly larger than ∼100 km). This size magnitude is within the range of the typical width of the SEMC, known to vary from 100 to 200 km, as shown by hydrographic measurements [*Schott et al*., 1988; *Donohue and Toole*, 2003]. Notice also that the width of ∼100 km of the SEMC is apparent in the ASCLME cruise data shown in Figure 5, which was also measured at 25°S. The model SEMC is surface intensified, with maximum velocities slightly above 0.7 m s^{-1}, which is in good agreement with the intensity of 80 cm s^{-1} estimated from in situ observations by *Donohue and Toole* [2003] and *Nauw et al*. [2008] at the same location. The model vertical extension of the SEMC at 25°S is deeper than that presented by *Nauw et al*. [2008] for the same latitude. However, other sections by *Nauw et al*. [2008] made slightly to the south of 25°S (see their Figure 2, transect T6), also shows the SEMC extending as deep as ∼1500 m (see their Figure 3, transect T6). The vertical structure of the SEMC observed through isopycnal perturbations of the neutral density field in the ASCLME cruise data, also suggests a vertical extension of the SEMC toward ∼1500 m depth (Figure 5d), which corroborates the model estimates.

Offshore of the SEMC, to the east of ∼48.5°E (Figure 3a), it was evident that there is a northward mean flow, with velocities ∼0.05 m s^{-1} penetrating to about 1000 m deep, but its main core with maximum velocity of ∼0.3 m s^{-1} was confined to the upper 300 m. Similar characteristics were also observed by *Nauw et al*. [2008], and appear to be linked with the flow of the SICC. Figure 3a also shows a northward flow below the SEMC, extending from 2000 m to the seafloor, and its maximum core was about 0.35 m s^{-1}, at the continental rise, between 3500 and 4000 m. The location of this northward flow is in agreement with the deep western boundary current along the east coast of Madagascar identified by *Donohue and Toole* [2003]. *Nauw et al*. [2008] have reported the presence of a northward flow below the SEMC, at intermediate depths, and termed it the East Madagascar Undercurrent (EMUC). The observed EMUC by *Nauw et al*. [2008] at 25°S has its core between 1000 and 1500 m, and lies over a steep continental slope. This is not evident in the model. This could be associated with the poor representation of the continental slope due to relatively coarse grid resolution (1/5°) of the model (it is instructive to compare Figure 3a with *Nauw et al*. [2008], their Figure 3, T8).

Figure 3b shows the vertical structure of the zonal mean flow at 45°E, from the Madagascar shelf to 30°S (Figure 2a for locations). The model also has been able to capture both the SEMC and SICC. Here the SEMC has a vertical extension of about 1000 m, maximum surface velocities of ∼0.4 m s^{-1}, and is confined to the north of ∼28°S. In contrast, the SICC has a maximum vertical extension of only ∼500 m, and maximum surface velocities of ∼0.15 m s^{-1}. While there is good agreement in general between the model and observations for the geographical location and vertical structures of the SEMC and SICC at 45°E, the model appears to under-estimate the magnitudes of their maximum intensity by ∼50%, when comparing it against hydrographic observations by *Nauw et al*. [2008] made at the same longitudinal position (see their Figure 3, T5). The vertical structure of the zonal extension of the SICC at 54°E, between 22°S and 29°S (Figure 3c), is comparable with the 1995 high resolution meridional hydrographic section from the World Ocean Circulation Experiment (WOCE) by *Siedler et al*. [2006] (their Figure 2, 54°E). At this position, SWIM captured the SICC, with its main core centered between 23°S and 24.5°S, confined to the upper 300 m (consistent with WOCE measurements, and findings by *Siedler et al*. [2006] and *Palastanga et al*. [2007]).

3.3. Mesoscale Activity

To evaluate the mesoscale activity from the model field, we have computed and mapped the Mean eddy kinetic energy ($MEKE = \overline{[u'^2+v'^2]}/2$) and compared it against that produced both by satellite altimetry and drifter data (Figures 4a and 4b). Both for model and altimetry, u' and v' are time fluctuations of horizontal components of geostrophic velocities derived from variations of SSH. For drifters, they account for variations of geostrophic and ageostrophic components of the flow. *MEKE* is known as a bulk measure of mesoscale activity [*Colas et al*., 2012]. Many studies have shown that the mesoscale activity in the Mozambique Channel and region around south of Madagascar are mainly dominated by eddies and rings [*de Ruijter et al*., 2002; *Schouten et al*., 2002a, 2003; *Ridderinkhof and de Ruijter*, 2003; *Halo et al*., 2014]. The Mozambique Channel is known as the most energetic area when compared with the region south of Madagascar. Such a pattern is also evident in Figure 4. There the drifters have shown a peak of *MEKE* ∼2000 cm^2 s^{-1}

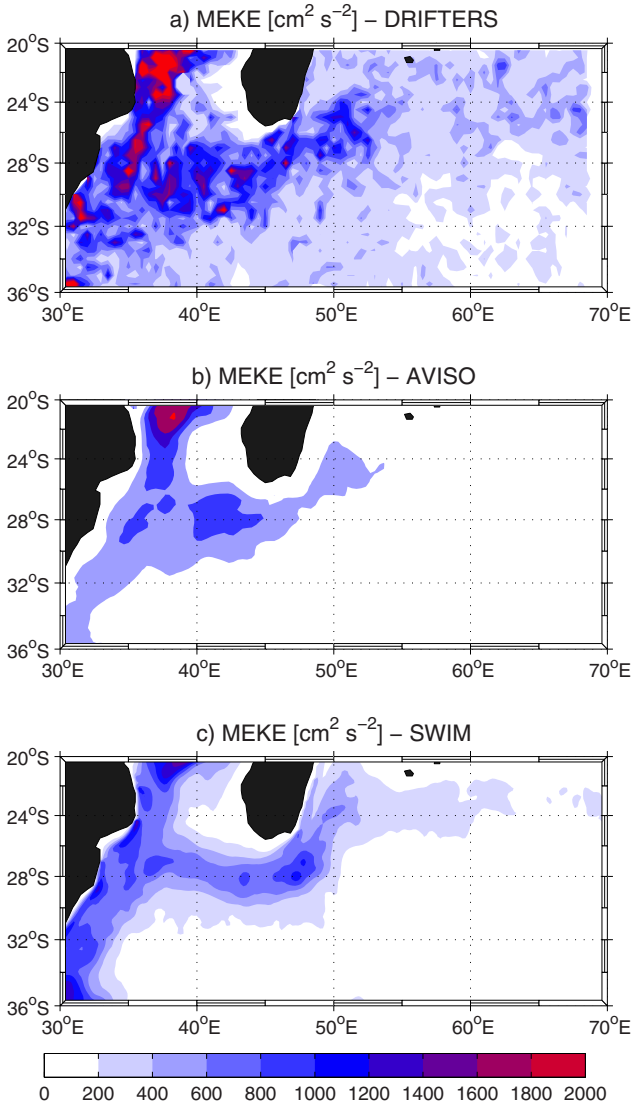

Figure 4. Surface mean eddy kinetic energy (*MEKE*). (a) Based on 215 drifters from 1992 to July 2012, (b) based on satellite altimetry from October 1992 to March 2010, and (c) Based on SWIM model 7 year climatology.

(Figure 4a), while altimetry has shown a peak ~1400 cm^2 s^{-1} (Figure 4b) and model ~1600 cm^2 s^{-1} (Figure 4c). South of Madagascar and along the southeastern African margin, both drifters and model produce peak values of about 1000 cm^2 s^{-1} and 1200 cm^2 s^{-1}, respectively, whereas altimetry only reaches a peak of ~800 cm^2 s^{-1} to the southwest of Madagascar, failing to produce the energetic field in the vicinity of the Agulhas Current. While in general all data sets agree with regard to their spatial distributions, the model appears to under-estimate the energy levels when compared against drifters, but over-estimates the altimetry. This is not a surprising result, as altimetric geostrophic velocities are known to under-estimate the ocean currents by about 30% [*Ternon et al*., 2014]. Processing of the altimetry data set requires grid interpolations and filtering of SSH field [*Chelton et al*., 2011b], thus reducing its local value. Drifters account for both geostrophic and ageostrophic components of the ocean currents. Recent analysis of the cyclogeostrophic balance in the Mozambique Channel has demonstrated that the main cause for the differences observed between altimetry and drifter EKE is associated with the omission of centrifugal acceleration in the geostrophic relation [*Penven et al*., 2014].

3.3.1. Eddy Density Structure

Figure 5 shows eddy field at two hydrographic transects during the ASCLME cruise in the southwest of Madagascar at 25°30S, in 26 and 27 August 2008, and in the southeast at 25°S, in 10 September 2008. In these sections, the flow has been integrated vertically in the upper 300 m of the water column. Altimetric maps of weekly sea level anomalies correspondent to the dates of the cruise were superimposed on the observed data. Thus, a clear pattern emerges: a strong cyclonic eddy is responsible for the clockwise reversal of the flow on the southwest transect close to Madagascar coast. The surface signal of this eddy appears to have a width greater than 200 km diameter. The expression of the SLA seems to under-estimate the diameter compared to the cruise data, likely due to interpolations in time and space, and processing of the satellite data. Nevertheless, there is good agreement between the two data sets. The pattern observed on the southeast coast shows a strong poleward flow along the Madagascar coast, the SEMC, and at its offshore edge an intense equatorward flow associated with a strong cyclonic eddy. The width of the observed current is slightly greater than 100 km, fairly consistent with other hydrographic data [*Schott et al*., 1988]. Because the ASCLME cruise track did not extend far offshore, the eddy was partly sampled, hence little can be inferred about its size. Bearing in mind that here the flow field is also dominated by the SICC [*Palastanga*

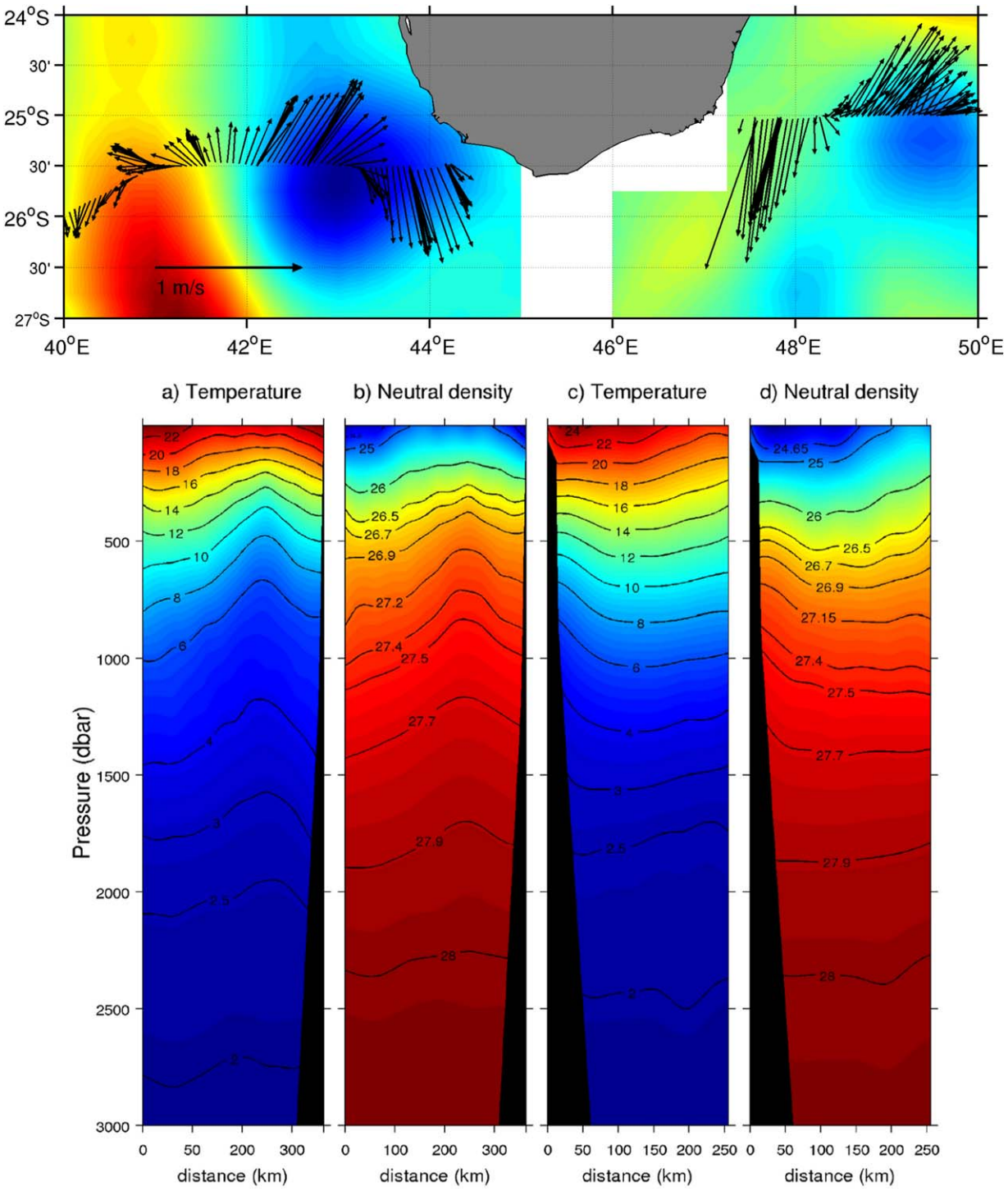

Figure 5. (top) Flow field of two cyclonic eddies, at the southwest of Madagascar, transect across 25°30S and at the southeast, transect at 25°S, measured by an ADCP during the ASCLME cruise in August and September 2008, respectively. The currents were integrated vertically in upper 300 m of water column, and superimposed on weekly maps of satellite observed sea level anomalies for the corresponding periods. Bottom plot shows their vertical structure obtained by CTD cast: (a) temperature and (b) neutral density at the southwest transect and (c) temperature and (d) neutral density at the southeast transect.

et al., 2007], the eddy mean flow interaction could have an influence on the observed pattern. Interestingly, the pattern produced here (Figure 5) resembles that observed in hydrographic measurements by *Donohue and Toole* [2003] (see their Figure 9), and the ACSEX cruise data presented by *Nauw et al*. [2006] (see their Figure 6), exactly at 25°S. The in situ observed eddy in the southwest transect showed a strong shoaling of

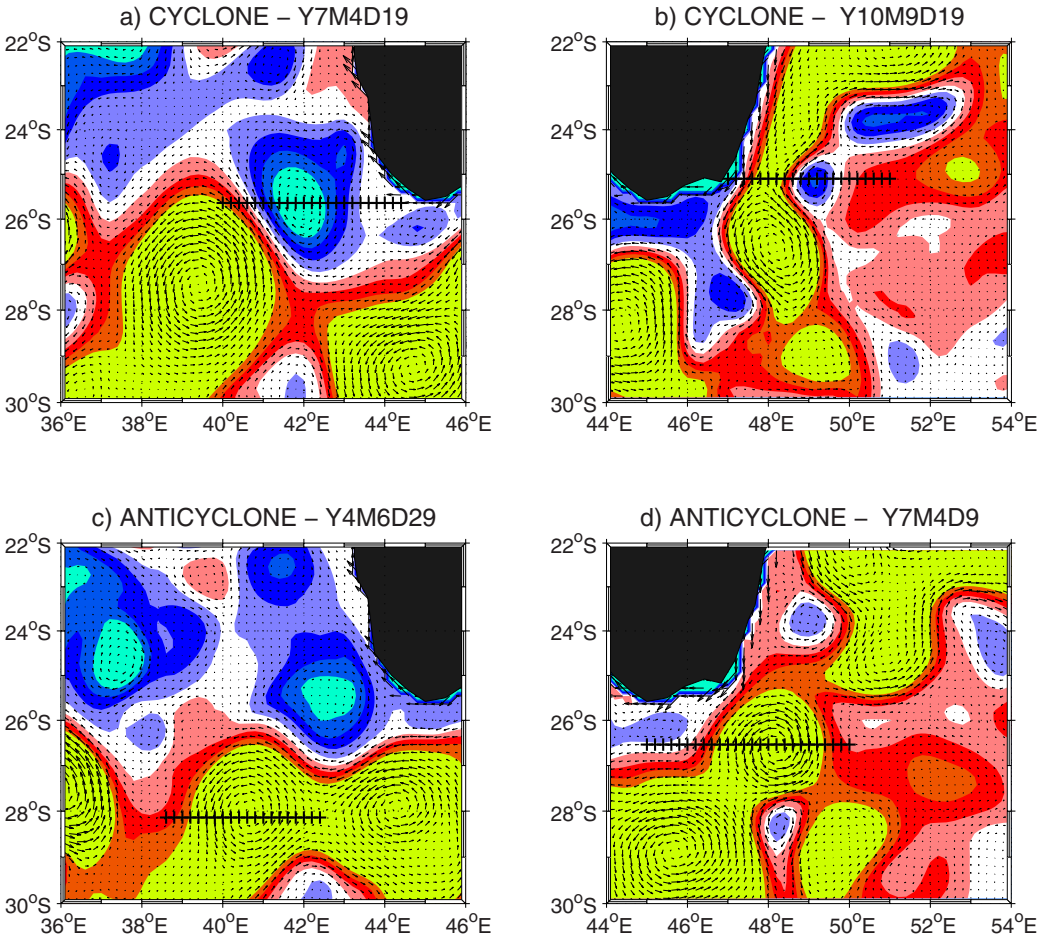

Figure 6. Model derived snap-shots of mesoscale eddy field computed from geostrophic velocities (m s^{-1}), based on SSH. The transects show positions used to inspect vertical structure of the eddies. (top, a) Cyclonic eddy captured in the southwest coast of Madagascar in 19 April, model year 7; (top, b) cyclonic eddy in the southeast of Madagascar, in 19 September, model year 10. (bottom, c) Anticyclonic eddy in the Mozambique Basin, in 29 June, model year 4, and (bottom, d) anticyclonic eddy in the southeastern coast of Madagascar, in 9 April, model year 7.

the isotherms, upwelling cooler deep waters to the subsurface layers. The maximum observed temperature at the sea surface was about 22°C (Figure 5a). Its density structure (Figure 5b) has shown stronger perturbations of the isopycnals between 500 and 2000 m, suggesting stronger eddy activity at subsurface layers. Horizontally, its core was centered about 200 km offshore. The transect in the southeast showed relatively warmer waters at the sea surface of about 24°C (Figure 5c), confined inshore (less than 150 km from the coast), suggesting a propagation of warm tropical waters by the SEMC. Further offshore, between 200 and 250 km, the shoaling of the isotherms was associated with a cyclonic eddy which caused upwelling. The transition depth from perturbed to flat isopycnals near 1500 m deep (Figure 5d) adjacent to the continental slope, sheds light on the vertical extension of the SEMC. Little can be inferred about the structure of the cyclonic eddy at the eastern margin of the SEMC (Figure 5d) because the transect only partly sampled the eddy field. Nevertheless, a radius greater than 150 km can still be observed.

To evaluate vertical structure of the eddies produced in the model, we have searched SWIM outputs for patterns resembling surface currents observed by the ASCLME cruise data (Figure 5). For the pattern in the southwest of Madagascar, the best case model scenario was found in 19 April, of the climatology year 7 (Figure 6a), while in the southeast it was for 19 September, year 10 (Figure 6b). The model density structure of the cyclonic eddies is shown in Figure 7. Top plot for the transect in the southwest and bottom plot for the transect in the southeast of Madagascar. Similarly for the anticyclones in Figure 8. The cyclone in the southwest had a temperature range between 4°C and 26°C in the upper 1500 m, being warmer inshore than offshore at the surface (Figure 7a). Maximum salinities were about 35.2 PSU, confined near the surface

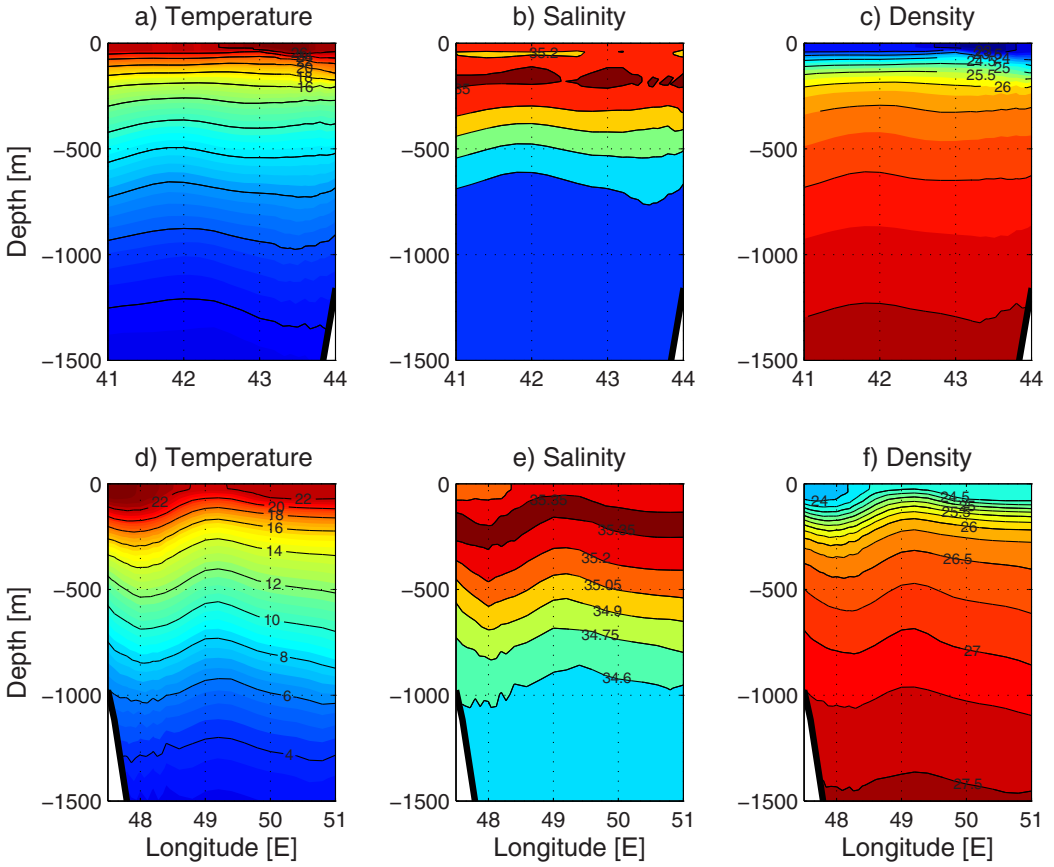

Figure 7. Vertical structures of cyclonic eddies in upper 1500 m. (a) Potential temperature (°C), (b) salinity (PSU), and (c) density anomaly (kg m^{-1}) of the cyclonic eddy captured in the southwest coast of Madagascar in 19 April, model year 7. On the other hand (d) temperature (°C), (e) salinity (PSU), and (f) density anomaly (kg m^{-1}) are for the cyclonic eddy in the southeast of Madagascar, in 19 September, model year 10 (see Figure 6, for their transects).

(Figure 7b). Potential density anomalies showed strong flat gradient of the isopycnals in the upper 250 m deep (Figure 7c). The cyclonic eddy in the southeast transect appears relatively stronger, evident by an intense perturbation of its properties. Minimum subsurface temperature 22°C, out-crops to the surface (Figure 7d). The eddy was fresher at the surface inshore, to the west of 48.5°E, and had a maximum subsurface salinity of 35.35 PSU confined in the upper 300 m (Figure 7e). The density structure (Figure 7f) has shown a strong shoaling of the isopycnals centered at 49°E, with intense gradients in the upper 300 m. Flat isopycnals adjacent to the continental slope, near 1500 m deep, appears to define the vertical extension of the SEMC. At the surface, the current transports relatively lighter (24.0 kg m^{-3}) water mass at the inshore. Its maximum temperature and salinity suggest the presence of tropical surface waters, known to be caused by intense precipitation over evaporation in the subtropics, advected southward by the EMC [*Tomczak and Godfrey*, 1994]. The structures of the anticyclones show a downwelling in the core of the eddy (Figure 8). The anticyclone in the southeast was relatively warmer, maximum temperature 26°C, at the surface (Figure 8d) than that in the southwest transects (Figure 8a). This feature of maximum temperature is associated with salinity of 35.2 PSU. Both eddies show subsurface maximum salinities of 35.35 PSU confined in the upper 300 m. Slopping of the isopycnal anomalies evident below 1500 m reveals that the eddy is also deep reaching (Figure 8d). Stronger gradient of the isopycnals in the upper 500 m indicates that the eddy is surface intensified.

3.3.2. Eddy Vertical Velocities

Because the ADCP cruise data only measured the upper 300 m of the water column, only the model field is used to investigate vertical velocity structures. Figure 9a shows model velocities of the cyclonic eddy captured in the southwest of Madagascar, at 25°50S, in 19 April, model year 7. The eddy was deep reaching ~3000 m, and exhibited velocities above 0.2 m s^{-1} in the upper 1000 m. The eddy had radius slightly

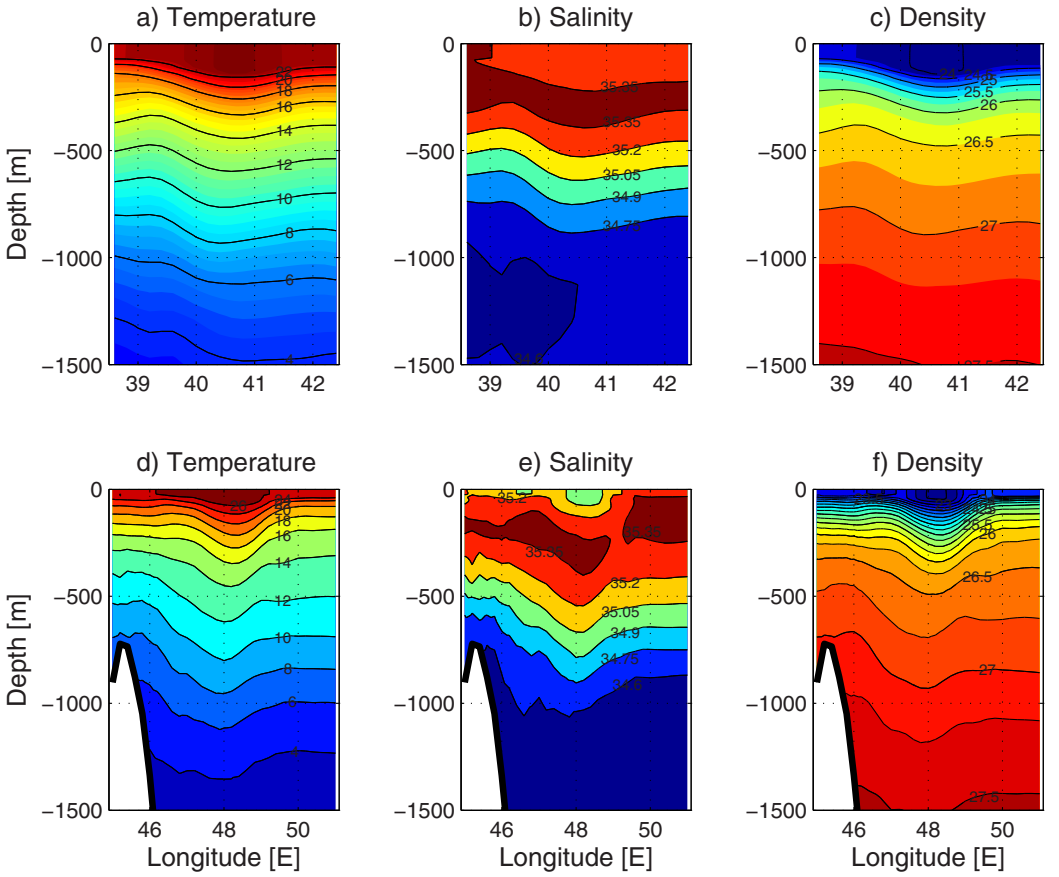

Figure 8. Vertical structures of anticyclonic eddies in upper 1500 m. (a) Potential temperature (°C), (b) salinity (PSU), and (c) density anomaly (kg m^{-1}) of the anticyclonic eddy captured in the southwest coast of Madagascar, in 29 June, model year 4. (d) Potential temperature (°C), (e) salinity (PSU), and (f) density anomaly (kg m^{-1}) of the anticyclonic eddy in the southeastern coast of Madagascar, in 9 April, model year 7 (see Figure 6, for their transects).

greater than 200 km. In contrast, the cyclonic eddy captured in the southeast coast in 19 September, model year 10 (Figure 9b) was relatively shallow, reaching a depth of about 1000 m, and smaller ∼150 km radius. It was surface intensified, with velocities above 0.2 m s^{-1} in the upper 500 m. At the inshore of this eddy, it was evident the SEMC, with a vertical extension of about 1500 m, as well as the bottom western boundary current with its core between 3000 and 4000 m deep, with maximum velocities of about 0.3 m s^{-1}. Note that both cyclonic eddies inspected here have their most intense velocities associated with the equatorward component. Figure 9c shows the anticyclonic eddy captured in 29 June, model year 4, in the Mozambique Basin. The eddy was large, ∼300 km diameter, strongly barotropic, reaching the bottom (∼4500 m deep). It exhibited velocities greater than 0.2 m s^{-1} in the upper 1000 m, with a poleward component more intense than its equatorward one. Likewise, the anticyclonic eddy captured in the southeast of Madagascar in 9 April, model year 7 (Figure 9d), also was large (nearly the same size ∼300 km radius). However, it was relatively shallower reaching a depth of about 1000 m, and it was strongly surface intensified. The eddy interacted with the SEMC, which also has shown a vertical extension of about 1500 m, consistent with in situ observations. Note also that the northward East Madagascar Bottom Current has been captured, lying over the continental slope, with maximum core of 0.2 m s^{-1} centered between 2800 and 4000 m deep.

4. Energy Conversion Terms in the Model

Because satellite altimetry observations are limited to the sea surface, we used SWIM output to obtain information throughout the water column to investigate the mechanisms of the eddy formation through instabilities of the currents. Following *Marchesiello et al.* [2003], we have computed two energy conversion terms derived from the volume-integrated evolution equation of the potential and kinetic energy budget, related

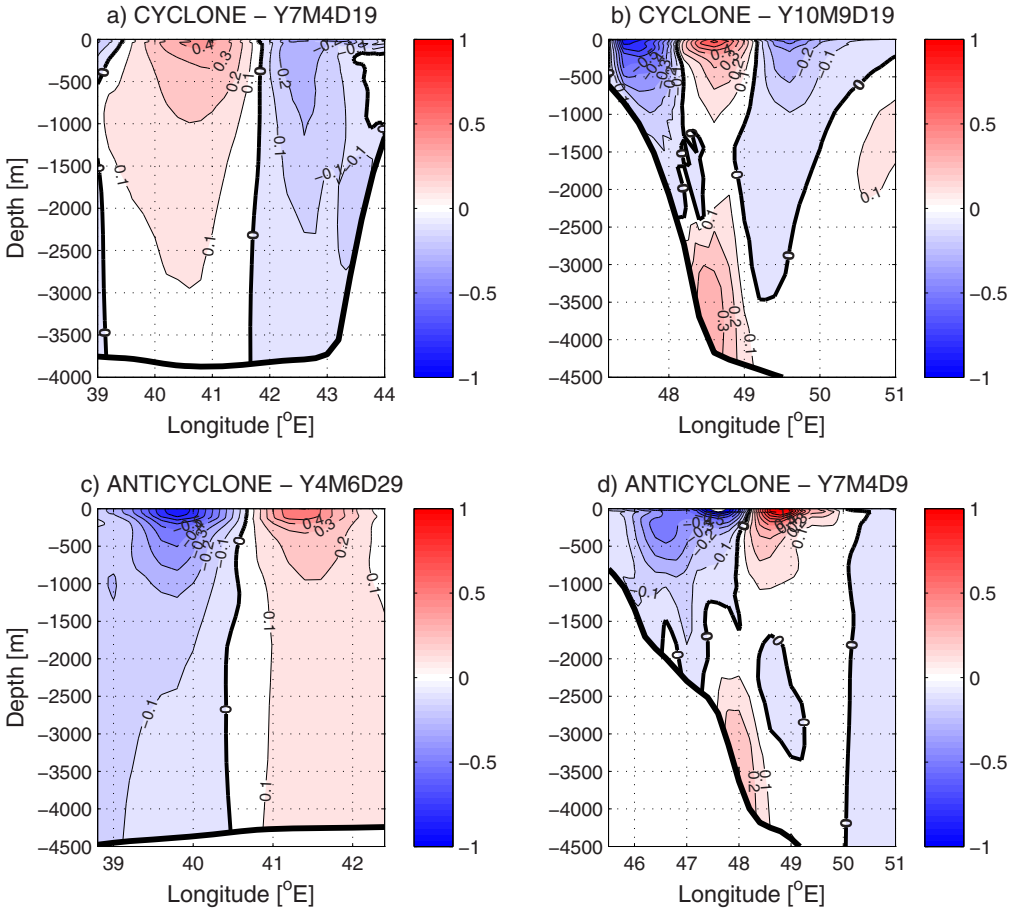

Figure 9. Vertical velocities structure (m s^{-1}) of cyclonic and anticyclonic eddies. (a) Cyclonic eddy captured in the southwest coast of Madagascar in 19 April, model year 7; (b) cyclonic eddy in the southeast of Madagascar, in 19 September, model year 10. (c) Anticyclonic eddy in the Mozambique Basin, in 29 June, model year 4, and (d) anticyclonic eddy in the southeastern coast of Madagascar, in 9 April, model year 7. Negative (positive) values denote poleward (equatorward) velocities (see Figure 6, for their transects).

to the source and sink of the oceanic eddy kinetic energy [*Kundu*, 1990; *Cronin and Watts*, 1996; *Azevedo et al*., 2008], expressed below:

$$KmKe = -\left[\overline{u'u'}\frac{\partial \bar{u}}{\partial x} + \overline{u'v'}\left(\frac{\partial \bar{u}}{\partial y} + \frac{\partial \bar{v}}{\partial x}\right) + \overline{v'v'}\frac{\partial \bar{v}}{\partial y}\right] \quad (1)$$

$$PeKe = \overline{-\rho' w'}\frac{g}{\rho_0} \quad (2)$$

where u', v' are the perturbations in time of the zonal and meridional components of the flow field, respectively, and $\bar{u}$ and $\bar{v}$ are the time-mean, and x, y, are zonal and meridional directions, respectively. g is the acceleration due to gravity, ρ' is the fluctuation of the seawater density, computed via nonlinear equation of state [*Jackett and McDougall*, 1995], ρ_0 is the seawater density of reference, and w' is the perturbation in time of the vertical velocity component. For derivations of the *KmKe* and *PeKe*, refer to the textbook by *Kundu* [1990], and other references [*Cronin and Watts*, 1996; *Azevedo et al*., 2008].

A similar approach was used by *Biastoch and Krauss* [1999] in the Mozambique Channel and in the Agulhas retroflection region. It also has been used to study the generation of the Natal Pulses (cyclonic meanders inshore of the Agulhas Current) [*Lutjeharms and Roberts*, 1988] at the Natal Bight [*Tsugawa and Hasumi*, 2010].

4.1. Barotropic and Baroclinic Instabilities

The energy transfer from mean kinetic to eddy kinetic defined by *KmKe* is an indicator of eddy formation through barotropic instabilities of the mean flow (provided it is positive). Otherwise, it represents eddy dissipation toward the mean flow [*Kundu*, 1990; *Biastoch and Krauss*, 1999].

The other transfer term defined by *PeKe* describes the conversion of energy from eddy potential to eddy kinetic "*buoyancy production*" [*Kundu*, 1990; *Marchesiello et al*., 2003]. It represents the work performed by turbulent buoyancy forces on the vertical stratification, leading to changes in potential energy [*Cushman-Roisin and Beckers*, 2009]. It is known as the second phase of baroclinic instability [*Kundu*, 1990; *Cronin and Watts*, 1996; *Marchesiello et al*., 2003; *Azevedo et al*., 2008].

The work of the local winds has been regarded less important for the mesoscale variability of this region [*Lutjeharms and Machu*, 2000], therefore here it is neglected.

5. Eddy Detection and Tracking Algorithm

The algorithm used to detect and track eddies combines both geometrical and dynamical properties of the flow field [*Halo*, 2012; *Halo et al*., 2014]. A geostrophic eddy is regarded as an instantaneous flow field identified simultaneously by closed contours of sea surface height (SSH) [*Chelton et al*., 2011b], and a negative Okubo-Weiss parameter [*Isern-Fontanet et al*., 2006; *Chelton et al*., 2007]. The Okubo-Weiss parameter [*Okubo*, 1970; *Weiss*, 1991] is defined as:

$$W = S_n^2 + S_s^2 - \xi^2 \tag{3}$$

where

$$S_n = \frac{\partial u}{\partial x} - \frac{\partial v}{\partial y} \tag{4}$$

$$S_s = \frac{\partial v}{\partial x} + \frac{\partial u}{\partial y} \tag{5}$$

$$\xi = \frac{\partial v}{\partial x} - \frac{\partial u}{\partial y} \tag{6}$$

S_n and S_s are the normal and shear components of strain tensor, respectively, ξ is the vertical component of relative vorticity, u and v are the geostrophic velocity components in x and y, respectively, derived from altimetric SSH:

$$u = -\frac{g\partial[SSH]}{f\partial y}, \quad v = \frac{g\partial[SSH]}{f\partial x} \tag{7}$$

g is the acceleration due to gravity, and f is the Coriolis parameter.

To minimize the subjectivity on the identification of the eddies, the algorithm is designed with a minimum tunable parameters: the intervals between the closed contours, set to 2 cm, and the maximum closed loop of SSH to exclude gyre-scale features, set to 600 km. The threshold value for W is 0. Two passes of the Hanning filter has been applied over W field to minimize the grid-scale noise, common in W methods [*Chelton et al*., 2011b; *Souza et al*., 2011]. As demonstrated by *Halo* [2012] and *Halo et al*. [2014], this hybrid method is more robust than using the closed contours method and the Okubo-Weiss criteria independently. The eddies are tracked with reference to their centers, following the method proposed by *Penven et al*. [2005], where an eddy retains its identity between two consecutive time steps when a generalized distance in a nondimensional property space is minimum.

6. Results and Discussions

The findings of the present study are presented and discussed below. These mainly include: the role of seasonality on eddy activity; the eddy generation processes, their seasonal cycle and spatial variability; the interaction of the eddies with the large-scale ocean currents in the region; the eddy demography and their mean properties.

6.1. Impact of Seasonality on Altimetry MEKE

To assess the overall impact of seasonal variations on the mesoscale activity, we have computed and mapped *MEKE* with and without seasonality included in the data set (Figure 10). Seasonality was removed by obtaining the anomaly from seasonal average [*Marchesiello et al*., 2003; *Penven et al*., 2005]. When seasonality was included in the data set there were two regions of enhanced *MEKE* located to the southeast

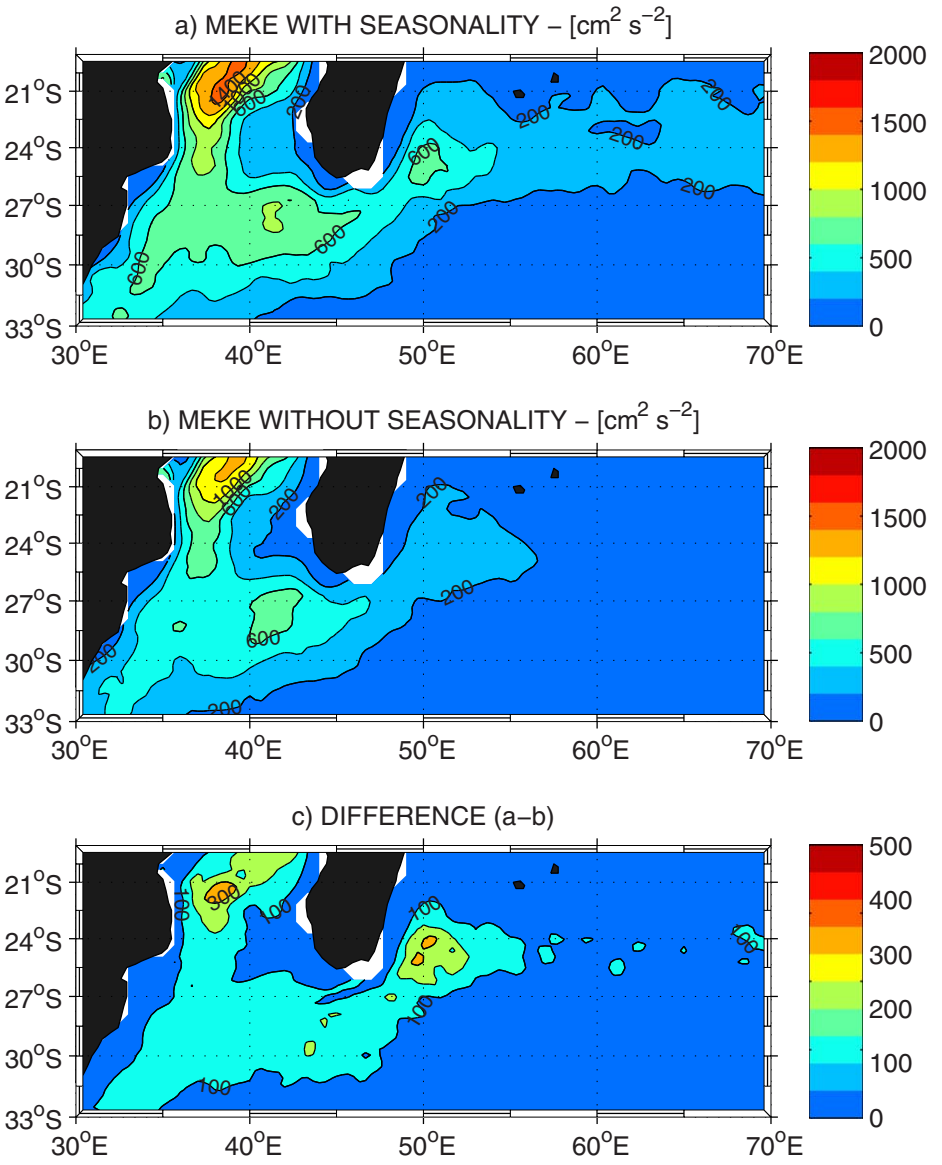

Figure 10. Mean eddy kinetic energy (cm^2 s^{-2}) computed from horizontal components of the geostrophic velocities derived from SSH. Data set extracted from AVISO for the period starting from 14 October 1992 to 31 March 2010. (a) Including the seasonality, (b) removing the seasonality, and (c) is the difference between with and without seasonality.

and southwest of Madagascar (herein SE and SW, respectively) (Figure 10a). The SW region lies in the Mozambique Basin, and had a local maximum *MEKE* of about 826 cm^2 s^{-2} centered around 27°S, 42°E. On the other hand, the SE region lies in the Madagascar Basin and had a local maximum *MEKE* of about 680 cm^2 s^{-2} centered around 25°S, 50°E. The pattern of the *MEKE* in the SE region with about 200 cm^2 s^{-2} extended zonally at approximately 24°S latitude to East of 70°E (Figure 10a). This pattern marks the presence of a corridor of SSH anomalies, also reported in various studies [*Schouten et al*., 2002b; *de Ruijter et al*., 2005]. This corridor has been previously attributed to the propagation of Rossby waves [*Birol and Morrow*, 2001; *Schouten et al*., 2002b; *Birol and Morrow*, 2003; *de Ruijter et al*., 2005]. However, findings from more recent studies strongly suggest that these are not waves, instead train of propagating mesoscale eddies [*Quartly et al*., 2006; *Chelton et al*., 2007], caused by baroclinic instabilities of the currents system within the subtropical South Indian Ocean [*Palastanga et al*., 2007].

When seasonality was removed from the data set, a reduction of the mesoscale activity was observed (stronger reduction in the SE region compared to the SW) (Figure 10b). The maximum *MEKE* in the SW was

about 676 $cm^2\ s^{-2}$ centered around 27°S, 42°E, and in the SE a maximum of about 384 $cm^2\ s^{-2}$ was centered around 25°S, 50°E. In this case, the pattern of the *MEKE* was confined to the west of about 55°E (Figure 10b). The difference between the *MEKE* with and without seasonality was calculated (Figure 10c). It indicates an overall impact of seasonal variations on the mean currents that accounts for 18% and 44% of the mesoscale activity in the SW and SE regions, respectively. By removing the seasonality (Figure 10b), the bulk effects of seasonal variations of the mean currents on the mesoscale activity are filtered out. The *MEKE* is influenced by variabilities at extraseasonal time scales. At these time scales, the subtropical eddy-corridor extended only to the west of about 55°E. This may suggest that the seasonal variations of the mean currents are strongly linked with variability produced in the far east Indian Ocean. The peak of *MEKE* observed near 24°S, 50°E (Figure 10a) suggests a local enhancement. Enhancement of eddy activity in this region has been attributed to the interaction of the arriving eddies from the east Indian Ocean [*Quartly et al*., 2006; *Palastanga et al*., 2007] with the SEMC at the southeastern slope of Madagascar [*Siedler et al*., 2009]. In the Mozambique Basin, the local maximum *MEKE* observed near 27°S, 42°E (Figure 10a) is relatively stronger than that observed in the Madagascar Basin (near 25°S, 50°E). In the latter region, the seasonality accounts for only 18% of the maximum *MEKE*, while in the former region it accounts for 44%. This indicates that a great deal of variability produced in the Mozambique Basin overwhelms that produced at seasonal time scales. The Mozambique and the Madagascar Basins are separated by the Madagascar Ridge, a prominent topographic feature rising up to about 2000 m depth (Figure 1a). It is thought that this bathymetric feature affects the mesoscale eddy variability observed in this region [*Quartly and Srokosz*, 2004], and is responsible for the two-distinct modes of variability to the west and east of 45°E [*Matano et al*., 1999, 2002]. *de Ruijter et al*. [2004] using LADCP measurements collected during the Agulhas Current Source Experiment cruise, combined with altimetric measurements observed a regular formation of mesoscale dipole eddies in this region. The period of enhanced formation of these dipoles coincided with the negative phase of the Indian Ocean Dipoles (IOD) and El-Ninõ Southern-Oscillation (ENSO) cycles [*de Ruijter et al*., 2004], which are phenomena at extraseasonal time scales.

In the next section, we investigate the dominant eddy forcing mechanisms through current instabilities, their seasonal cycle and geographical distribution.

6.2. Model Derived Barotropic and Baroclinic Instabilities, Their Seasonal Cycle

To study the barotropic (*KmKe*) versus baroclinic (*PeKe*) contribution in the eddy formation, vertical profiles of the energy conversion terms within the region of enhanced mesoscale variability (39°E–51°E and 32°S–23°S, Figure 10a) were inspected for different seasons of the year: December–February (DJF), March–May (MAM), June–August (JJA), and September–November (SON). The seasons used here are in agreement with the criteria used by *Lutjeharms et al*. [2000], where DJF is representative of summer season, MAM is for fall, JJA is for winter and SON for spring.

6.2.1. Model Derived Vertical Structures of KmKe and PeKe

Figures 11a and 11b show the characteristic mean-profiles for *KmKe* and *PeKe* averaged within the region. DJF (dotted lines), MAM (dashed lines), JJA (dot-dashed lines), and SON (continuous lines). The profiles of *KmKe* show large seasonal variations at the sea surface, ranging from $\sim -4 \times 10^{-8}\ cm^2\ s^{-3}$ during fall to $2 \times 10^{-8}\ cm^2\ s^{-3}$ during winter. The seasonal variations are confined to the upper ocean, above 300 m (Figure 11a). The merging of the *KmKe* profiles toward 0 $cm^2\ s^{-3}$ observed below 300 m depth (Figure 11a) suggests that regardless of the season, almost no eddies were formed through barotropic instabilities below this depth, and *KmKe* could be neglected.

PeKe has a relatively smaller amplitude range of seasonal fluctuations (Figure 11b). The individual profiles have more oscillations compared to *KmKe*, both in the upper ocean (0–500 m) and at intermediate depths (between 800 and 2000 m) (Figure 11b), suggesting two different layers of enhanced *PeKe* variability. The upper layer had maxima extremes of $\sim -3.5 \times 10^{-8}\ cm^2\ s^{-3}$ during spring season, near 200 m depth, and $\sim 1 \times 10^{-8}\ cm^2\ s^{-3}$ during winter season, near the surface (Figure 11b). At intermediate depths, the maximum extreme was also $\sim 1 \times 10^{-8}\ cm^2\ s^{-3}$ during winter season, at about 1300 m. The oscillation of the *PeKe* profiles above and below zero (Figure 11b) indicates that the eddy energy was transferred between its kinetic and potential state (vice versa) through baroclinic instability. By comparing *KmKe* against *PeKe* in the upper 300 m depth, it was evident that the amplitudes of *KmKe* were greater than the *PeKe*, especially in winter. On the other hand, at intermediate depth, the amplitudes of *PeKe* were greater than the *KmKe*

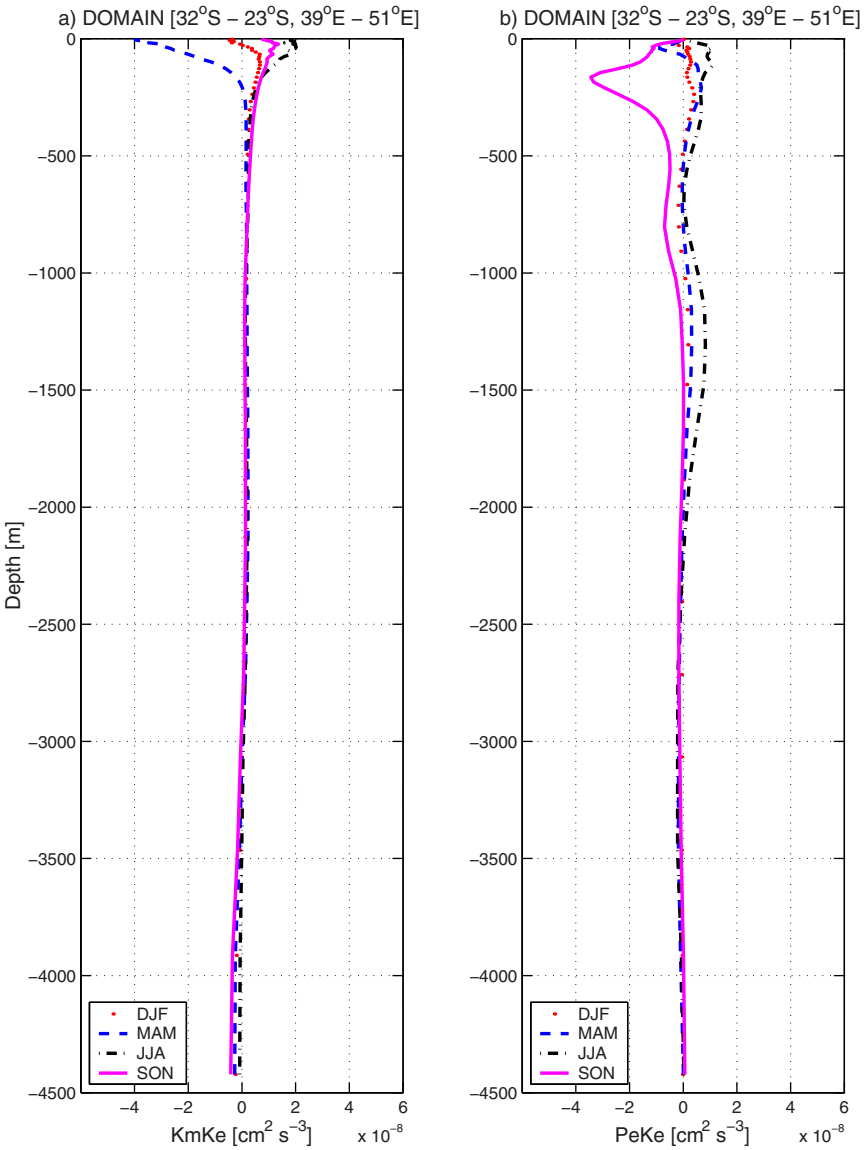

Figure 11. Mean-vertical profiles of energy conversion terms indicating both (a) barotropic (*KmKe*) and (b) baroclinic (*PeKe*) instabilities of the flow field at different seasons: December–February (DJF), March–May (MAM), June–August (JJA), and September–November (SON), averaged between 39°E and 51°E, and 32°S and 23°S.

(evident for fall and winter seasons). This suggests that both *KmKe* (at the surface) and *PeKe* (at intermediate depth) were important mechanism for the formation of eddies in the region.

In the next section, we inspect the relative importance of the eddies toward the general oceanic circulation of the region, which provides evidence of the linkage between SEC and SICC.

6.2.2. Impact of Eddies on the Model Derived Mean Flow

The contribution of the eddies toward the mean flow was determined from the negative profiles of *KmKe* (*KmKe* < 0), following *Biastoch and Krauss* [1999]. The strongest signal of negative *KmKe* was observed in the upper 300 m during MAM (Figure 11a), which indicates that the contribution of the eddies toward the mean flow is significant only during fall season. *Siedler et al.* [2009] have investigated the contribution of the SEMC toward the SICC, using floats injected in the background flow field derived from NEMO model. They found that the SEMC contributes 40% of the total volume flux of the SICC, through a retroflection of the SEMC. However, it has been claimed that a retroflection of the SEMC has not been observed with in situ measurements, furthermore is thought that it does not exist [*Ridderinkhof et al.*, 2013]. Our results indicate that the connection

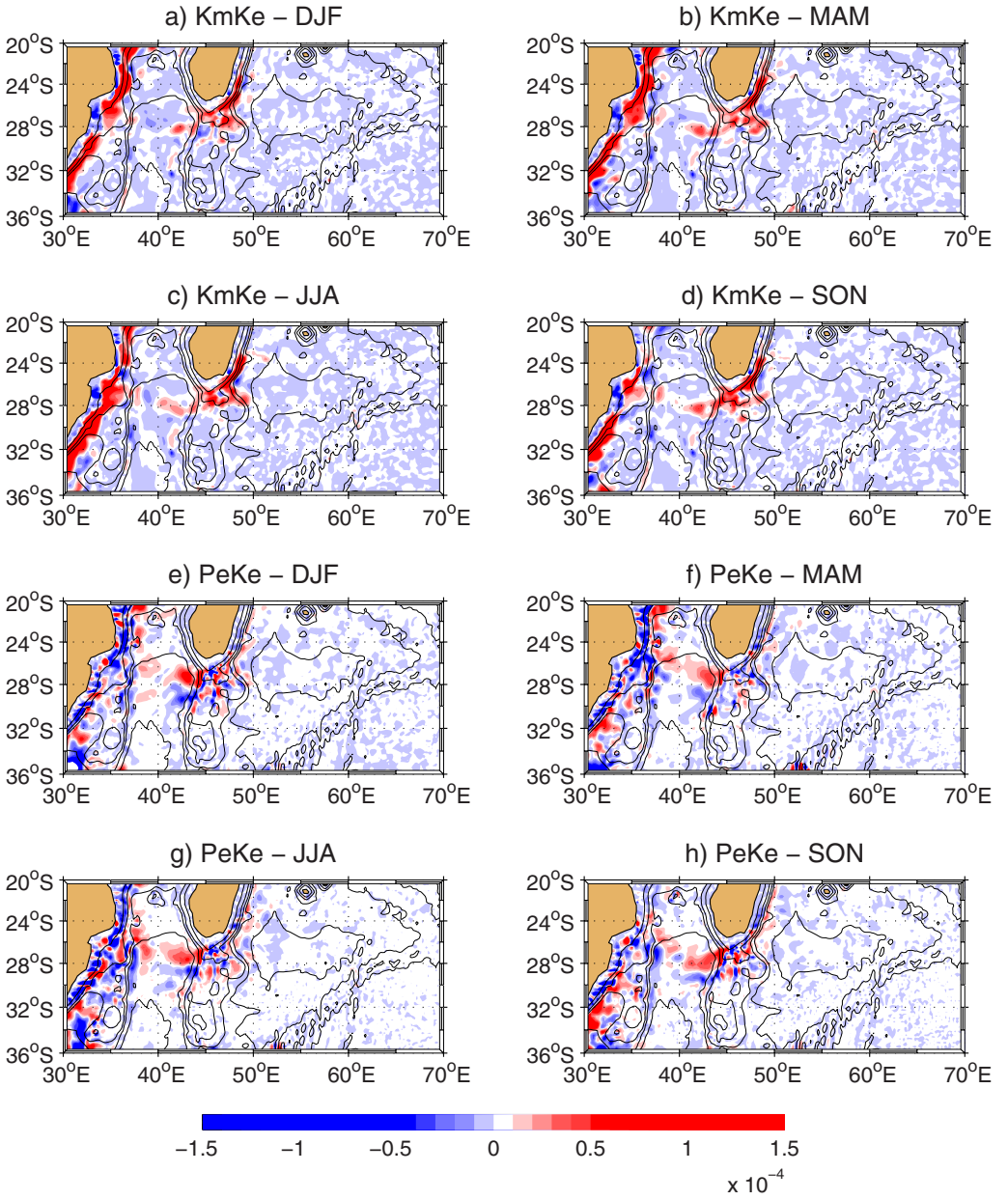

Figure 12. Eddy generation by barotropic (*KmKe*) and baroclinic instabilities (*PeKe*) in different seasons: December–February (DJF), March–May (MAM), June–August (JJA), and September–November (SON). The maps are vertically integrated throughout the water column.

between SEMC and SICC is likely to be established through the shedding of anticyclonic eddies. This conclusion would be consistent with a nonpersistent retroflection of the SEMC, stated by *Quartly et al.* [2006]. A small contribution from the eddies toward the mean flow was also observed below 3500 m depth, for all seasons (Figure 11a). This may suggest a marginal, but persistent contribution of the eddies toward the deep currents.

To diagnose the geographical focus of eddy formation through current instabilities, spatial maps of eddy conversion terms were prepared and are presented in the next section.

6.2.3. Model Derived Spatial Distribution of KmKe and PeKe

To investigate the spatial variability of the conversion terms, we plotted seasonal maps of *KmKe* and *PeKe* (Figure 12). The maps were constructed by vertically integrating *KmKe* and *PeKe* throughout the water column. Patches of high positive *KmKe* and *PeKe* indicate enhanced eddy formation. Otherwise indicates

eddy dissipation toward the mean kinetic energy and toward the eddy potential energy, respectively. Regions of enhanced eddy formation were found near the southern coast of Madagascar throughout the year. *KmKe* dominates to the southeast of Madagascar (Figures 12a–12d), and *PeKe* on the southwest (Figures 12e–12h). The strongest *KmKe* in the region was observed along the African coast, stretching from the Mozambique Channel toward the Agulhas Current region (Figures 12a–12d). This pattern is consistent with the altimetry derived *MEKE* (Figure 10). Along the SEMC the strongest signal of *KmKe* was mostly located near the Madagascar continental shelf, at the southeastern sector of the island, suggesting strong shear production in the SEMC. This is not a surprising result. In this region, patches of *KmKe* are located where a great-deal of mesoscale disturbances occurs when the SEMC approaches the southeastern edge of Madagascar continental shelf [*Lutjeharms*, 1988; *Lutjeharms and Machu*, 2000; *de Ruijter et al*., 2004; *Siedler et al*., 2009]. *de Ruijter et al*. [2004] found that such disturbances of the flow field have the potential for causing an anticyclonic recirculation and a possible localized retroflection of the SEMC, which may favor the formation of anticyclonic eddies. Results from our numerical model suggest that these anticyclonic eddies are formed through the transfer of kinetic energy from the mean component to eddying component, shear production in the southward flowing SEMC. In the southwest of Madagascar, eddy formation appears to be driven by both barotropic and baroclinic instabilities of the westward propagating SEMC, after it has past the southern tip of Madagascar (Figure 12). It is likely that some eddies are formed through coastline and topographic effects.

The maps of *PeKe* highlight local enhancement of eddy formation between the southern tip of Madagascar continental shelf and the Madagascar Ridge (the outflow region of the SEMC), throughout the seasons, lying in the northeastern sector of the Mozambique Basin, between 26°S and 20°S (Figures 12e–12f). Along the African continent, the signals of *PeKe* stretching from the Mozambique Channel toward the Agulhas Current region are noisy and rather difficult to interpret. However, it is evident that negative *PeKe* dominated on the continental shelf, while positive *PeKe* appeared to dominate slightly off-shelf, suggesting that the continental shelf in this region may also contribute for the dissipation of eddy kinetic energy toward its potential form. This pattern of dissipation at the western boundary is consistent with *Zhai et al*. [2010] (see their Figure 3), which appears to be the main region of eddy dissipation in the Indian Ocean.

An interesting feature appears when comparing *KmKe* (Figures 12a–12d) against *PeKe* (Figures 12e–12h) for each corresponding season. The respective distribution of *PeKe* and *KmKe* structures located at the outflow region of the SEMC, and on the western flank of the Madagascar Ridge, near 44°E, 28°S, indicates that baroclinic instabilities dominated to the north of 28°S, relatively closer to the Madagascar shelf, while barotropic instabilities dominated to the south of that latitude. This pattern was consistent throughout the seasons. Strongly positive and negative patches of *PeKe* are located at the outflow of the SEMC (Figures 12e–12h). Similar structures, but for an instantaneous flow field was observed and investigated in the Cape Verde Frontal Zone, using in situ measurements from a moored current meter and numerical solution from an isopycnal coordinate model [*Erasmi et al*., 1998]. The results infer that such patterns are produced when passing eddies induce a vertical displacement of the isopycnals and a disturbance of the vertical velocity field. They also suggest that cyclonic eddies moving through a less disturbed background flow, it is expected that a large positive *PeKe* will be located at the leading edge of the eddy, and a large negative *PeKe* at the back. The opposite will be observed in case of an anticyclonic eddy [*Erasmi et al*., 1998]. In our case, the direction of propagation of the eddies generated in the outflow of the SEMC is mainly southwestward. The large negative patches of *PeKe* of the time-averaged field (Figures 12e–12h), located to the south of the positive patches, arguably would suggest a predominant propagation of anticyclonic eddies. Notwithstanding, *de Ruijter et al*. [2004] and *Ridderinkhof et al*. [2013] have found that the anticyclonic part of the dipole structure formed in this region is generally the first to form over its cyclonic counter-part.

In the next section, we investigate the relationship between the eddy forcing mechanisms and the intensity of the dominant large-scale circulation feature, thus providing evidence of the drivers of the eddy variability.

6.3. Relating Model Derived Seasonal Cycle of KmKe and PeKe With Volume Transport of the SEMC

To infer possible mechanisms related with the seasonal variability on the eddy formation, we have quantified the mean of the energy conversion terms in the upper 1000 m of the water column for different seasons and compared against the corresponding volume transports. The energy conversion terms were

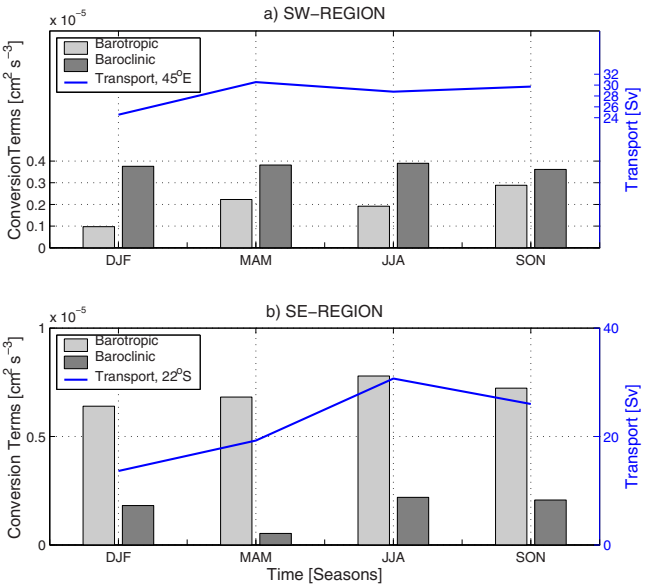

Figure 13. Seasonal cycle of *KmKe* (light-gray) and *PeKe* (dark-gray), and volume transport. (a) Estimated in the southwest of Madagascar between 39°E and 45°E, and 32°S and 23°S, and (b) southeast of Madagascar between 45.10°E and 51.10°E, and 32°S and 23°S. The volume transport in Figure 13a was estimated at 45°E, and in Figure 13b was estimated at 22°S. For both the conversion terms and the transports were calculated integrating vertically through the upper 1000 m of the ocean column.

quantified at two-distinct regions, characterized by the most intense mesoscale eddy variability, both the southwest of Madagascar, in the Mozambique Basin (between 39°E and 45°E, 32°S and 23°S), and in the southeast of Madagascar, lying in the Madagascar Basin (between 45°E and 51°E, 32°S and 23°S) (Figure 1a). The transports were estimated at two different locations: at 22°S, between 48°E and 51°E, across the poleward SEMC proper, and at the southern tip of Madagascar, at 45°E, between 25°S and 30°S (Figure 1a). At this site, the westward flow of the SEMC is known to receive tributaries from the recirculation of the subtropical gyre of the southwest Indian Ocean [*Stramma and Lutjeharms*, 1997], and flow variability (Rossby waves and/or eddies) from the far east Indian Ocean [*Schouten et al*., 2002b; *de Ruijter et al*., 2005; *Quartly et al*., 2006]. Figure 13 shows their corresponding relationship. In Figure 1a, the boxes marked SW and SE indicate southwestern and southeastern region, respectively. The northernmost limit of the region was made at 23°S and the westernmost limit was at 39°E to avoid the inclusion of eddies from the Mozambique Channel. The longitude 45°E separating the SE and SW regions seemed to be a well-chosen position as it lies along the crest of the Madagascar Ridge (Figure 1a), and has been shown to separate distinct modes of variability to the west and east of Madagascar Ridge [*Matano et al*., 1999]. The southern limit was chosen to prevent the inclusion of the eddies originating from the Agulhas Return Current [*Lutjeharms and Ansorge*, 2001; *Lutjeharms*, 2006]. It is likely that the results within these regions can be sensitive to the degree of inclusion of eddies with different characteristics from those locally generated, depending on the lateral sizes of the regions. Baroclinic instabilities (dark-gray bars) dominated in the SW region (Figure 13a), while barotropic instabilities (light-gray bars) dominated in the SE region (Figure 13b). In the SW region, the seasonal cycle of *PeKe* has shown almost no seasonal variation, and never was above 0.4×10^{-5} cm^2 s^{-3} (Figure 13a). The contribution of *KmKe* was relatively lower throughout. It has shown high seasonal variations, with minimum of $\sim 0.1 \times 10^{-5}$ cm^2 s^{-3} observed during summer, and maximum of $\sim 0.3 \times 10^{-5}$ cm^2 s^{-3} during spring. The superimposed line in Figure 13a represents the seasonal cycle of the volume transport estimated at 45°E. It showed small variability, and varied in phase with *KmKe*. The minimum transport was ~24.6 Sv during summer, and maximum of ~30.60 Sv during fall season. In the SE region, the seasonal cycle of *KmKe* showed relatively larger amplitudes, but with small variations. A minimum of $\sim 0.64 \times 10^{-5}$ cm^2 s^{-3} was observed during summer, and maximum of $\sim 0.8 \times 10^{-5}$ cm^2 s^{-3} during winter (Figure 13b). The contribution of *PeKe* was lower throughout. A minimum of $\sim 0.05 \times 10^{-5}$ cm^2 s^{-3} was observed during fall season, and a maximum of $\sim 0.21 \times 10^{-5}$ cm^2 s^{-3} during winter. The superimposed line in Figure 13b represents the seasonal cycle of the volume transport of the SEMC at 22°S. It showed high seasonal variations, with minimum transport of ~13.64 Sv during summer season, and maximum of ~30.69 Sv during winter. The seasonal cycle of the transport has shown a significant phase variation with *KmKe*.

The results indicate that *KmKe* varied in phase with the transport estimates for both SW and SE regions. This suggests prevalence for eddy formation by barotropic instabilities, strongly linked with the seasonal intensification of the SEMC. A connection between eddy formation and transport variability also has been observed between Mozambique Channel eddies and the pulsing flow of the SEC, at the Cape-Amber, the

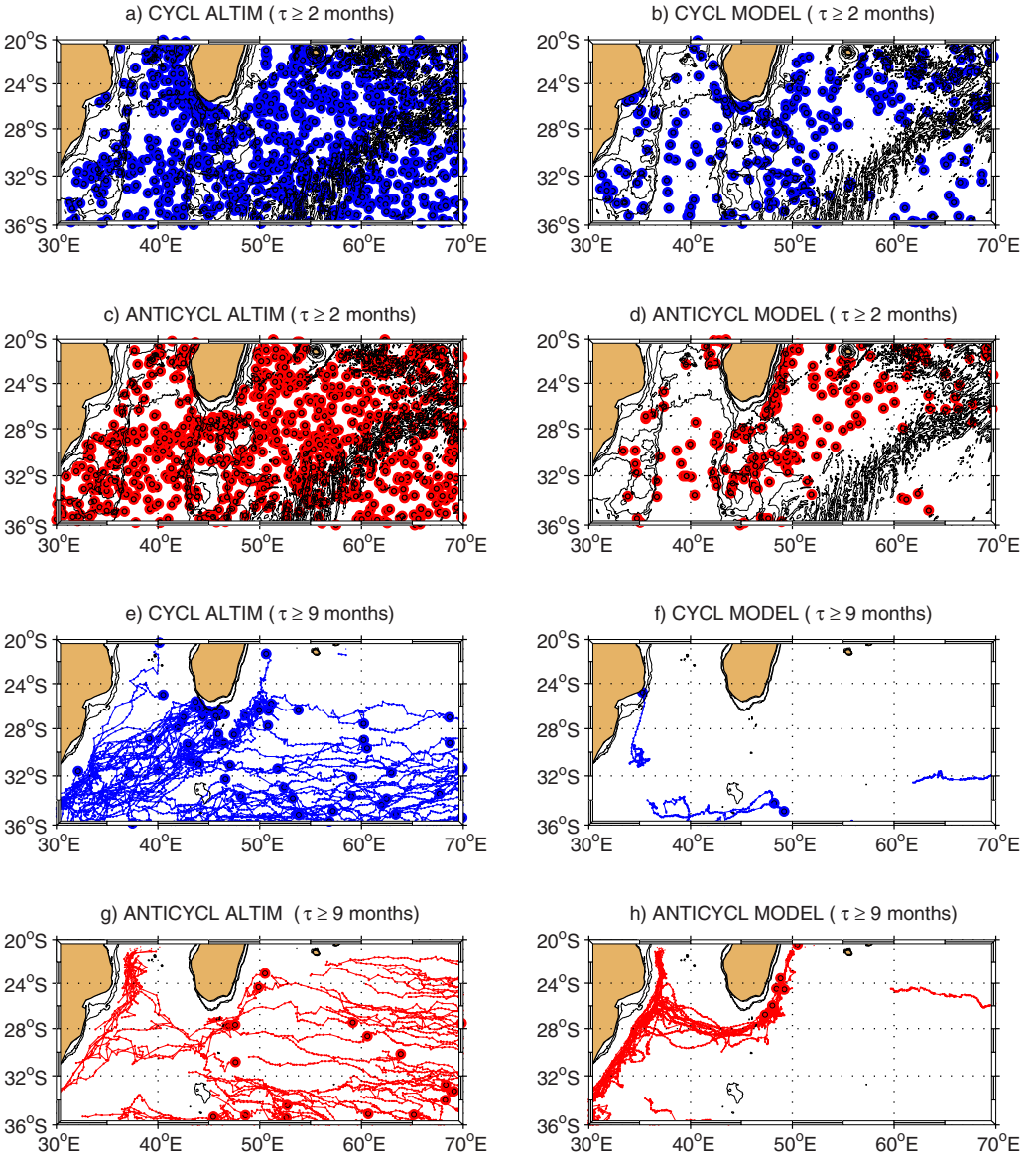

Figure 14. (left) Eddy generation sites identified from altimetry for the period ranging from 14 October 1992 to 31 March 2010, and (right) from the model, 7 years. Cyclones (blue) and anticyclones (red). Only eddies with a life-time of 2 months and greater are presented. The coastal isolines indicate the isobaths of 500, 1000, 2000, 3000, and 4000 m from GEBCO1 data set. From Figures 14e–14h, only trajectories of long-lived eddies (life-time of 9 months and greater) are shown for visualization purposes. Only the isobaths 500 and 1000 m are shown.

northern tip of Madagascar [*Backeberg and Reason*, 2010]. Intensification of the currents system in the region has been attributed to the seasonally varying forcing of the gyre circulation, linked with the variability of the wind field over the south Indian Ocean Basin [*de Ruijter et al*., 2005; *Palastanga et al*., 2007]. Surprisingly, *Nauw et al*. [2008] using velocity estimates from altimetric sea level anomalies from 1993 to 2005, found no evidence for a seasonal variation in the transport rate of the SEMC linked with the seasonal variability of the wind field over the Indian Ocean.

To quantify the eddies formed in the region, a demographic study of the eddies has been performed and are presented in the next section.

6.4. Eddy Demography From Altimetry and Model Data

Eddy demography was determined using the automatic eddy detection and tracking algorithm described in section 5. The algorithm was applied to both weekly maps of absolute dynamic topography produced by AVISO, from 14 October 1992 to 31 March 2010, and model outputs for 7 years. While the eddies were

identified in the whole domain (Figures 14a–14d), the analysis of the statistical census and mean properties (occurrence, kinetic energy, diameter, amplitude, vorticity, life-time, maximum traveling distance, polarity, and nonlinearity) were limited to the regions of most intense variability, SW and SE (Figure 1a for reference).

6.4.1. Eddy Birth

Figures 14a, 14c and 14b, 14d show generation sites of all cyclonic and anticyclonic eddies with a life-time of 2 months and greater ($\tau \geq 60$ days) in the altimetry and model data, respectively. Looking at the spatial distribution of the generation sites in both products, it is evident that both cyclonic and anticyclonic eddies were generated almost everywhere. In fact, it is now known that mesoscale eddies are ubiquitous features in the ocean [*Chelton et al*., 2007, 2011b]. Nevertheless, it is also observed in the two data sets a preferential tendency for cyclonic eddies to be formed directly south and southwest of Madagascar coast, near the continental shelf (Figures 14a and 14b), while the anticyclonic eddies generally formed slightly farther offshore (Figures 14c and 14d). The generation of cyclonic eddies near to the coast was also observed to the south of the La-Reunion Island (∼22°S, 55°E), and over the African continental shelf, near the Delagoa Bight (∼26°S, 33°E). Within the Mozambique Channel, to the north of ∼24°S, both cyclones and anticyclones appear to be generated mostly in the eastern boundary. It is interesting to see that the model also feature this pattern remarkably well, giving us further confidence in the model. The occurrence of eddies near Madagascar and the African coast, over the Mozambican shelf (Figures 14e–14h), is an indicative of continental boundary effects. In the southwestern Madagascar shelf (Figure 14e, near 26.5°S, 43.5°E), the distribution of cyclonic eddy formation sites is in agreement with the description of the flow found in recent literature [*de Ruijter et al*., 2004; *Siedler et al*., 2009; *Ridderinkhof et al*., 2013]. These studies have suggested that an occlusion of a cyclonic recirculation from the SEMC, near the southwestern sector of the Madagascar shelf triggers cyclonic eddies, by friction between the landward edge of the SEMC with the shelf. On the other hand, the seaward edge of the SEMC becomes unstable, leading to an anticyclonic recirculation, eventually triggering anticyclonic eddies, which may form a part of a dipole structure [*de Ruijter et al*., 2004], hence explaining the presence for the site of anticyclonic eddy formation, here observed in both products directly south and southwest of Madagascar. Whereas along the eastern margin of the African continent, over Mozambican shelf, the generation of cyclonic eddies is in agreement with the Delagoa Bight eddies described by *Lutjeharms and da Silva* [1988], known to be formed by interaction of the flow from the Mozambique Channel, with the continental slope [*Lutjeharms and da Silva*, 1988; *Lamont et al*., 2010]. The anticyclonic eddy formation along the southeastern margin of Madagascar near 28°S appears to be related to the interaction of the SEMC with the local topography (Madagascar Ridge), perhaps during the period when the SEMC is mostly poleward oriented as proposed by *Siedler et al*. [2009]. On the other hand, the generation site at 24°S could be related to the interaction between the SEMC with the incoming variability signals from the Indian Ocean, along the eddy-corridor [*Quartly et al*., 2006] (see Figure 1b). These patterns are also evident in altimetry (Figure 14g) and model (Figure 14h).

Caution is required when comparing the maps of energy conversion terms by *KmKe* and *PeKe* presented in Figure 12 against the eddy birth sites identified by the eddy detection scheme used here as shown in Figure 14. The latter shows generation sites almost everywhere, while the former shows *KmKe* and *PeKe* at localized positions. Both model and observations clearly show that for some places, high clusters of eddy birth sites are located where strong signals of *KmKe* and/or *PeKe* cooccurs (e.g., along the southeastern coast of Madagascar, also around the southern tip of Madagascar). On the other hand, there are also clusters of high birth positions where no signals of *KmKe* and/or *PeKe* are enhanced (e.g., clusters of cyclonic eddies along the southwestern margin of Madagascar, between 26°S and 24°S). Such an apparent discrepancy should be interpreted carefully: the energy transfer terms being vertically integrated, they will be significant for eddies generated with a sufficient vertical extension. The eddy detection being done on the surface pressure field (the SSH), it does not discriminate between structures purely at the surface and those with a larger vertical extension. This is probably why there is a better correspondence with the long-lived eddies (a structure with a larger spatial extension should be able to keep its coherence for a longer time).

6.4.2. Eddy Census

For the entire period of altimetry used here (14 October 1992 to 31 March 2010), the eddy detection scheme in the SW region identified a total of 394 eddies. About 58% of these were cyclones and 42% were

Table 1. Mean Eddy Properties Estimated in Two-Different Regions Around South of Madagascar, Southwest Region, SW: 39°E–45°E and 32°S–23°S, and Southeast Region, SE: 45.10°E–51.10°E and 32°S–23°S (See Figure 1a for Reference)[a]

	SW Region		SE Region	
Properties	Cyclones	Anticyclones	Cyclones	Anticyclones
AVISO				
N_{eddies}	229	165	175	181
L	145 ± 21.0	150 ± 33.0	139 ± 28.0	154 ± 32.0
η	15.0 ± 7.0	15.0 ± 8.0	9.0 ± 4.0	12.0 ± 7.0
ζ	−1.1 ± 0.3	0.92 ± 0.22	−0.83 ± 0.39	0.79 ± 0.28
f	−6.93 ±0.64	−6.95±0.55	−6.94 ± 0.64	−6.82 ± 0.65
τ	176 ± 105	126 ± 85	163 ± 109	142 ± 93
λ	827 ± 457	617 ± 437	550 ± 418	585 ± 460
MODEL				
N_{eddies}	42	64	65	80
L	124 ± 11	178 ± 26.0	120 ± 14	166 ± 22.0
η	9.0 ± 4.0	28.0 ± 18.0	9 ± 5.0	22.0 ± 12.0
ζ	−0.93 ± 0.3	1.16 ± 0.2	−1.10 ± 0.34	1.20 ± 0.35
f	−6.7 ± 0.62	−6.87 ± 0.66	−6.82 ± 0.65	−6.79 ± 0.65
τ	90 ± 29	183 ± 104	144 ± 54	153 ± 94
λ	415 ± 229	1052 ± 744	325 ± 195	777 ± 659

[a]Estimates made from altimetric eddies detected from 14 October 1992 to 31 March 2010, and model output (7 years). Neddies is the number of eddies, L (km) is eddy diameter, η (cm) is eddy amplitude, ζ ($\times 10^{-6}$ s^{-1}) is the relative vorticity, f ($\times 10^{-5}$ s^{-1}) is Coriolis parameter within the eddy, τ (day) is eddy life-time, and λ (km) is the maximum eddy traveling distance.

anticyclones. In the SE region, it identified a total of 356 eddies, of about 49% cyclonic and 51% anticyclonic. Whereas in the model (for 7 years), in the SW region, a total of 106 eddies were found: about 60% were anticyclones and 40% were cyclones. On the other hand, in the SE region, a total of 145 eddies were found, about 55% were anticyclones and 45% were their counter-part. Table 1 shows their statistical census *N*. Relatively smaller quantities found in the model as opposed by altimetry product could be related to the fact that model time series is shorter. Dividing the total number of the eddies by the number of years in altimetry (∼17.47 years), the estimates suggest that there are about 13.1 cyclonic and 9.4 anticyclonic eddies generated per annum in the SW region, and 10 cyclonic and 10.4 anticyclonic eddies generated in the SE region. In the model, for SW region there were about 9.14 anticyclones and 6 cyclones per year, while in the SE region there were about 11.4 anticyclones and 9.3 cyclones formed per year. These estimates are slightly above from that reported in previous studies, where a total of 4–6 eddies per year are proposed [*de Ruijter et al*., 2004; *Ridderinkhof et al*., 2013]. Higher estimates in our case could be related to the use of relatively more precise algorithms to identify mesoscale eddy structures. It is important to keep in mind that the estimates by *de Ruijter et al*. [2004] and *Ridderinkhof et al*. [2013] were made specially for dipole-eddies, while here that is not the case.

To assess the general characteristics of the eddies dominating the region an inspection of their relevant mean geometrical and dynamical properties are presented below.

6.4.3. Eddy Mean Properties From Altimetry and Model: Size, Amplitude, Vorticity, Life-Time, and Traveling Distance

Knowledge of eddy size, amplitude, vorticity, life-time, and traveling distances can provide information on eddies behavior, and allows one to infer their implication both on the overall ocean circulation, and ecosystems response. These properties have been estimated and are presented in Table 1 (diameter $\bar{L}$, amplitude $\bar{\eta}$, relative vorticity $\bar{\zeta}$, planetary vorticity $\bar{f}$, life-time $\bar{\tau}$, and maximum traveling distance $\bar{\lambda}$), derived from altimetry and model, for the SW and SE regions. The eddy equivalent mean diameter ($\bar{L}=2\times\sqrt{\sum S/N\pi}$) was defined as the mean of all identified eddies per frame [*Souza et al*., 2011]. Where *S* is the eddy's surface, assumed to have a circular geometry, and *N* is the total number of eddies detected. The eddy amplitude was defined as the difference between the highest and lowest SSH within the eddy [*Chelton et al*., 2011b]. The mean eddy relative vorticity ($\bar{\xi}=\sum \xi/N$), for the SW and SE regions was computed from the horizontal geostrophic components of the flow field: $\xi=\partial v/\partial x-\partial u/\partial y$. The annual mean eddy properties in the SW and SE regions as observed by altimetry (Table 1) shows a general tendency for more cyclones to be formed in the SW and anticyclones in the SE region. On the other hand, the model shows anticyclonic dominance everywhere. In terms of $\bar{L}$ and $\bar{\eta}$, the cyclones are more comparable to anticyclones in the SW than in the SE region. Again this is not present in the model results. Symmetry between the mean sizes of cyclones and

anticyclones in the SW region also has been observed by *de Ruijter et al.* [2004] and *Ridderinkhof et al.* [2013]. The estimates shown in Table 1 indicate that the model slightly over-estimates the size of the anticyclones, while under-estimating the cyclones. It also greatly over-estimates the amplitude of the anticyclones. Over-estimation of the eddies amplitudes could be associated to the fact that the model over-estimates the variability of SSH in this region, as demonstrated in our previous study [*Halo et al.*, 2014]. While over-estimating the eddy-size presented in Table 1, one should keep in mind that in situ observation made in this region have shown that the eddies radii in the region varies from 50 to 250 km [*de Ruijter et al.*, 2004]. The swirling velocities of the eddy observed during the ASCLME at the southwest coast of Madagascar, around 25°30S (Figure 5), also can give an idea of the size of the eddy. These observations suggest that the eddies presented here (Table 1), are within the expected range. Altimetric results presented in Table 1 have shown that cyclonic eddies formed in the SW region have stronger vorticity, live longer, and travel longer distances from their origin than any other mesoscale coherent structure inspected. However, the model failed to reproduce that pattern, while attributing such properties to the anticyclones. Nevertheless, these results indicate that the eddies in the SW region hold distinct properties from those in the SE. It is tempting to relate such differences to the different modes of variability which are known to dominate these regions, namely, seasonal wind forcings to the west of the Madagascar Ridge, and current variability to the east [*Matano et al.*, 1999].

6.4.4. Eddy Tracks

Figures 14e–14g show the trajectories of cyclonic and anticyclonic eddies derived from the altimetry and model data. The dots represent their generation sites and the tracks their pathways. Only long-lived eddies ($\tau \geq 9$ months) are presented for visualization purpose. For this time scale, there are more long-lived eddies in the altimetry (Figures 14e and 14g), than in the model (Figures 14f and 14h). In altimetry there are more long-lived cyclones than anticyclones, while the opposite is observed in the model. From the altimetry, many of the long-lived cyclonic eddies formed directly south of the southern tip of Madagascar (Figure 14e), made their way toward the southeastern coast of the African continent. This indicates that connectivity between Madagascar and Africa does exist. Whereas for anticyclones (Figure 14g), such connectivity still exist, but is not vigorous at this time scale. In the model, such time scale favors more anticyclones (Figure 14h) than cyclones (Figure 14f). For both products, the long-lived anticyclonic eddies were formed only to the east of ∼45°E, in the Madagascar and Mascarene Basins. These eddies propagate predominantly westward, with a slightly northwestward orientation for anticyclones (Figure 14g). Westward propagation of eddies with a slight meridional deflections (poleward for cyclones and equatorward for anticyclones) is in agreement with a previous study in the region [*de Ruijter et al.*, 2004], (see their Figure 9). These trajectories are consistent with theories of geostrophic ocean turbulence [*McWilliams and Flierl*, 1979; *Chelton et al.*, 2007], and have been observed in various ocean basins [*Morrow et al.*, 2004]. Eddies meridional deflections have been attributed to a combined effect of the planetary vorticity gradient and eddy self-advection [*McWilliams and Flierl*, 1979; *Cushman-Roisin*, 1994]. Altimetric cyclones and anticyclones have been deflected poleward at the continental boundary, in the southeastern coast of Madagascar. In coastal zones, meridional deflections are known to be associated with background boundary currents [*Chelton et al.*, 2011b]. In our case, the SEMC and the AC may play a significant role. From the model, at the time scale ($\tau \geq$ 9 months), none eddy from the east Indian Ocean was able to reach the Madagascar coast. They dissipate near 60°E (Figures 14f and 14h). In the Mozambique Basin, eddies have followed a southwestward trajectories, with cyclones having a stronger poleward orientation than anticyclones. Again, it is also evident a northwestward propagation of the anticyclones from altimetry (Figure 14g) and model (Figure 14h). On reaching the African continent at ∼24–25°S, they seem to be advected poleward along the path of the eddies and rings coming from the Mozambique Channel, which are known to propagate parallel to the coast toward the Agulhas Current [*de Ruijter et al.*, 2002; *Schouten et al.*, 2003; *Ridderinkhof and de Ruijter*, 2003; *Halo et al.*, 2014].

6.4.5. Eddy-Density and Energy Distribution

Figures 15a–15d shows the distribution of the total number of eddies (in %) with $\tau \geq 60$ day, identified in the SW and SE regions, in the altimetry data set (from 14 October 1992 to 31 March 2010), and model output (for 7 years). They are distributed as function of their radii, clustered at 10 km intervals. The corresponding eddy kinetic energy integrated across their surface is shown from Figures 15e–15h. For the altimetry, cyclonic eddies are represented by white bars and anticyclonic eddies by black. Whereas in the model, cyclones are light-gray bars, and anticyclones are dark-gray. Eddies with radii smaller than 40 km are

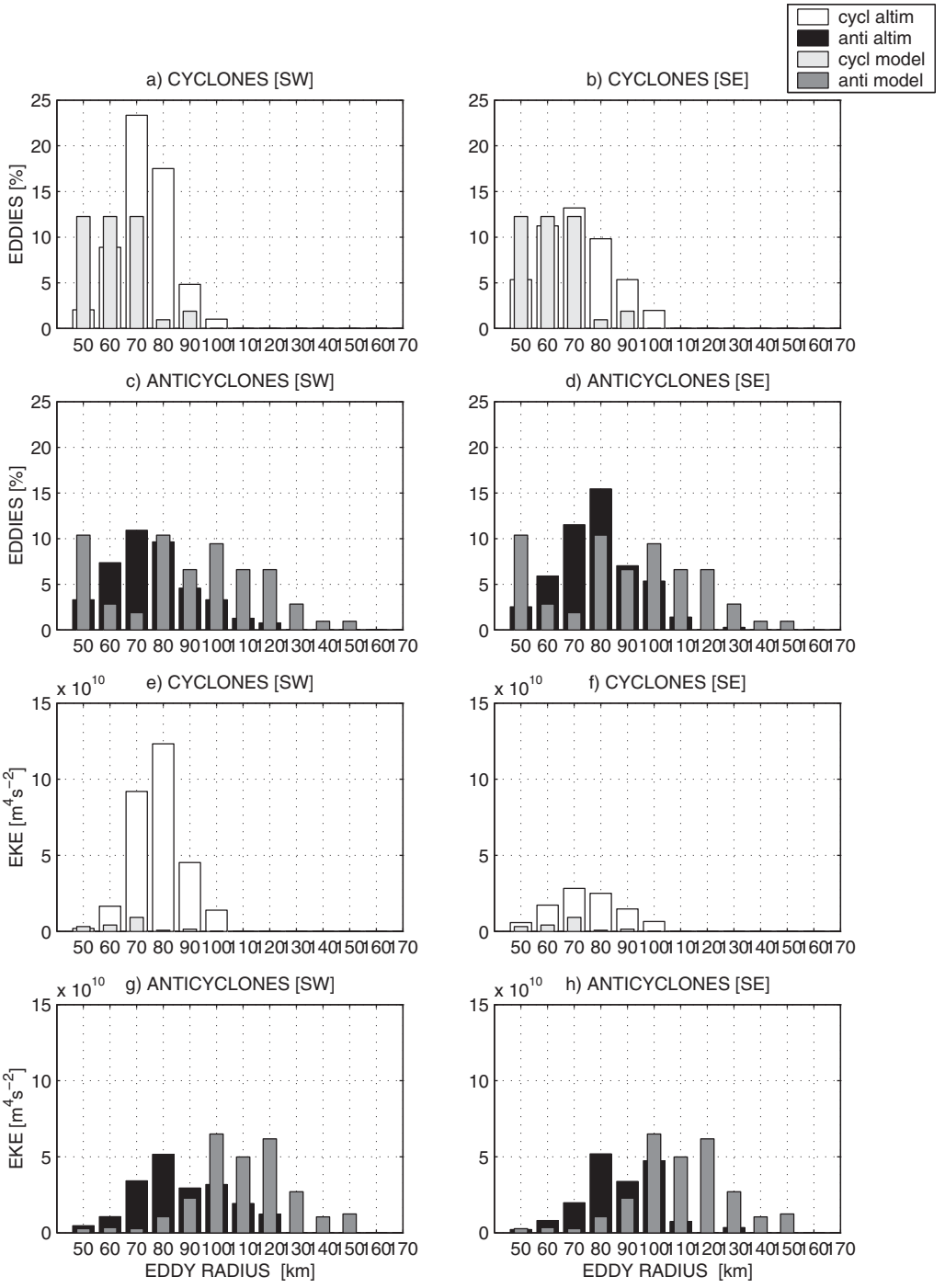

Figure 15. Distribution of the total number of selected eddies (%) and eddy kinetic energy ($m^4\ s^{-2}$) as function of their radii (km). Left (right) plots represent SW (SE) regions. For altimetry: cyclones (white bars) and anticyclones (black bars), for eddies detected from 14 October 1992 to 31 March 2010. For the model: cyclones (light-gray) and anticyclones (dark-gray) from the 7 years output. Only eddies with a life-time $\tau \geq 60$ days are considered. SW: 39°E–45°E, 32°S–23°S, and SE: 45.10°E–51.10°E, 32°S–23°S (see Figure 1a for reference).

generally unresolved by the gridded altimetry product [*Chelton et al.*, 2011b; *Everett et al.*, 2012]. Therefore, here for the two products, eddies radii smaller than 50 km were omitted from our analysis to prevent the inclusion of potential grid-scale artifacts.

For the altimetry, eddies radii in the SW region ranged from 50 to 100 km for cyclones (Figure 15a), with dominant peak centered at 70 km, in a nearly normal distribution. On the other hand, the radii of the

anticyclones span from 50 to 120 km (Figure 15c). Likewise, their dominant peak was centered at 70 km radii, slightly skewed to the left. For the model, cyclones radii ranged from 50 to 90 km, and exhibited a peak at multiple scales (50–70 km), and the anticyclones varied from 50 to 150 km radii, with peaks at 50 and 80 km. In the SE region, the eddies derived from altimetry ranged also from 50 to 100 km for cyclones (Figure 15b), with peak centered at 70 km radius, in a near-normal distribution. Their counter-part had radii ranging from 50 to 130 km (Figure 15d), and had their peak centered at 80 km radius, also in a near-normal distribution. On the other hand, in the model, the cyclones ranged from 50 to 110 km, with peak at 60 km radii. The anticyclones ranged from 50 to 160 km, and the peak was also skewed to 60 km radius. These size estimates corroborates the results in Table 1, which suggests that the anticyclones were generally larger than cyclones. *Chelton et al*. [2011b] found that more than 90% of eddies in the global ocean have a horizontal scale that ranges from 50 to 150 km, thus the eddy-sizes estimated by our algorithm are within the expected range.

With regard to the surface integrated eddy kinetic energy (Figures 15e–15h), it is observed by altimetry that in the SW region, the most energetic eddies (Figure 15e) had a radii of 80 km (more energy in cyclones than anticyclones). While the eddies in the model had their peak at 70 km. Here the energy is almost totally under-represented (Figure 15e). In the SE region, the anticyclones from altimetry (Figure 15h) were more energetic than the cyclones (Figure 15f). The same is true also in the model. The energy peak of the observed cyclonic eddies was centered at 70 km radius, and for the anticyclones it was at 80 and 100 km. Cyclonic eddies generated in the SW region (Figure 15e) appeared to be the most energetic features in the system. The peak of energy of the anticyclonic eddies in the SW region at 80 km radii is almost equal to that observed in the SE region.

The integrated eddy kinetic energy (Figures 15e–15h) indicates that the cyclonic eddies in the SW region are the most energetic structures inspected (Figure 15e). The maximum peak is $\sim$3 times greater than in the SE region. Comparatively, no significant difference is observed between the anticyclonic eddies of the two regions. In the SW region, the eddy radius at which most energetic eddies occurs is at 80 km, for both cyclones and anticyclones. In the SE region, maximum energy occurs at 70 km radius for cyclones and at 80 km radius for anticyclones. Here a second energy peak also occurs at 100 km radius (Figure 15h). Eddies radii at 80 and 100 km are relatively larger than the first baroclinic Rossby radius of deformation for this region, which ranges from 40 km in the south to 60 km in the north [*Chelton et al*., 1998]. This result may suggest that the sizes of the dominant eddies formed here are not controlled by the internal radius of deformation.

From the model, the energy peak of the cyclonic eddies both in the SW was at 70 km, and in the SE region was from 60 to 80 km radii. The model did not reproduce the energetic of the cyclonic eddies in these regions. Even more so in the SW than in the SE region. Most of the energy of the eddies produced in the model are retained in the large anticyclones. In the SW the energy peak was centered at 100 km radii, while in the SE region it was at 110 km radii. In fact, the energy of the anticyclones in the model is higher than that produced by altimetry. Eddies with radii beyond the first baroclinic Rossby radius of deformation have been regularly observed in this region, from both in situ and satellite altimetric observations [*de Ruijter et al*., 2004; *Quartly and Srokosz*, 2004; *Nauw et al*., 2006].

To infer where observed eddies with a certain characteristic length-scale are more likely to be formed, we computed and mapped the spatial distribution of the eddy mean radius from altimetric data set, as presented by *Penven et al*. [2005] (their Figure 15b). They are presented and discussed below.

6.4.6. Spatial Distribution of the Eddy Radii, Amplitude, and Life-Expectancy Derived From Altimetry

Figures 16a and 16b show the spatial distribution of the eddy radii, for cyclonic and anticyclonic eddies, respectively. The dominant length-scale of cyclones and anticyclones was $\sim$70 km. The generation of larger ($R \geq 90$ km) cyclonic eddies (Figure 16a) was less observed when compared against the anticyclonic eddies (Figure 16b). Near the south coast of Madagascar, the anticyclonic eddies were much smaller ($\sim$50 km radius) than the cyclonic eddies ($\sim$70 km radius). Along the African continent, both cyclones and anticyclones showed smaller radii, likely due to the frictional effects of continental boundary.

The spatial distribution of the averaged eddies radii with respect to their origin for cyclones (Figure 16a) and anticyclones (Figure 16b) shows distinct patterns. Directly south of Madagascar, at the inshore edge, the cyclonic eddies are larger than the anticyclonic eddies. The same is true at the southeast coast of

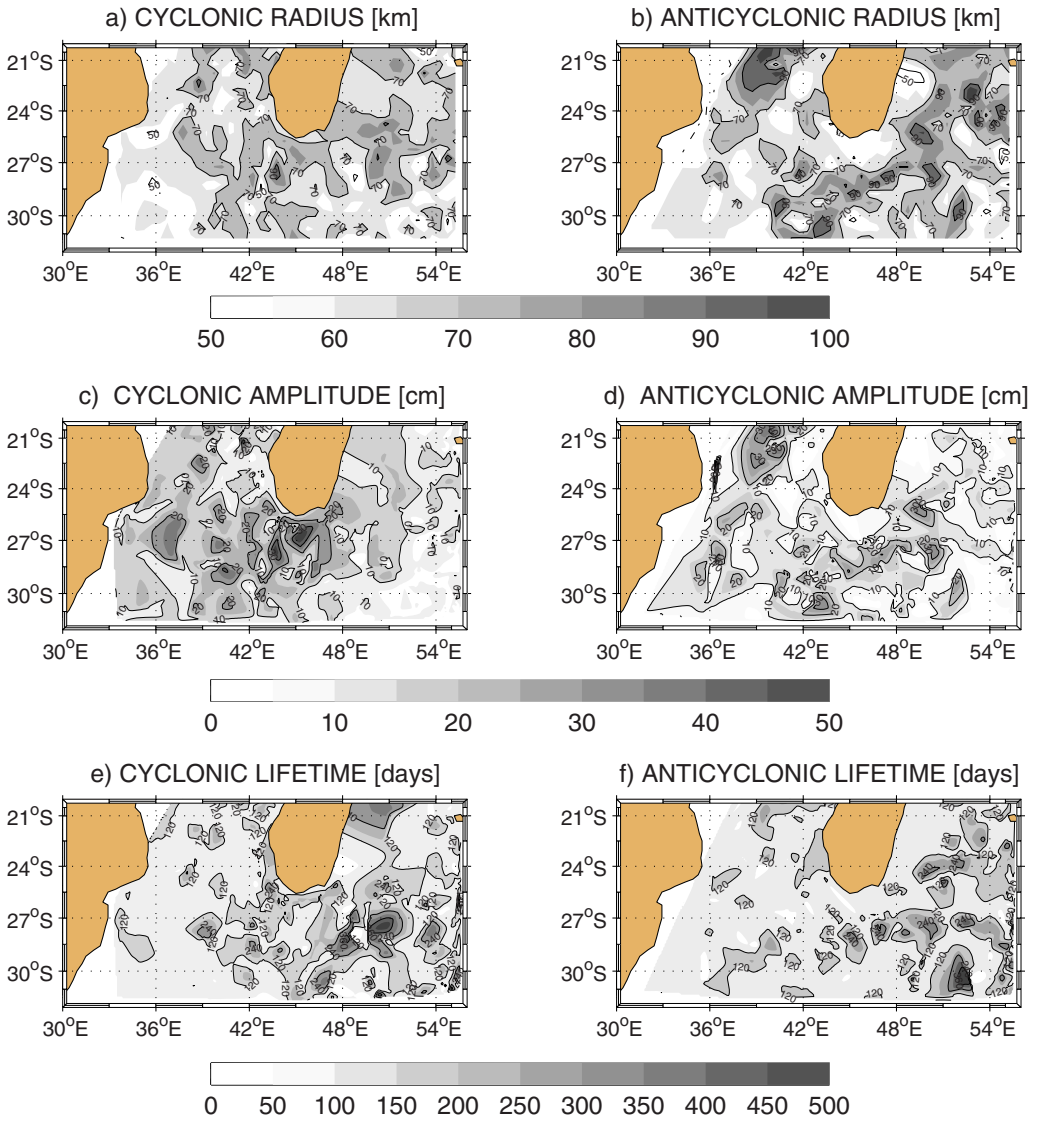

Figure 16. Spatial distribution of the mean eddy radius (km), mean amplitude (cm), and mean time of eddy permanence (days), with regard to their generation site. Altimetric eddies detected from 14 October 1992 to 31 March 2010. Left plots show cyclonic eddies and right plots anticyclonic.

Madagascar. However, the opposite is observed further offshore. This may suggest a larger sensitivity for dissipation of the anticyclones by frictional effects with the continental boundaries. Their life-expectancy also corroborates further this conclusion (Figures 16e and 16f). Another distinct pattern is a general tendency for the eddies to decrease in size from the south of Madagascar toward the southeastern African coast. From geostrophic oceanic turbulence, such a poleward meridional decrease of the eddies horizontal scale is expected to occur, since the deformation radius decreases with the increasing latitude [*Chelton et al*., 1998, 2007].

Similar analysis also made for the spatial distribution of the eddy mean amplitude, for cyclonic and anticyclonic eddies, as presented by *Everett et al*. [2012] for the Tasman sea (see their Figures 1c and 1d), is shown in Figures 16c and 16d, respectively. Comparing these maps against their corresponding plots (Figures 16a and 16b), a consistent pattern is observed: the position of the highest mean amplitude (∼over 30 cm) of the cyclonic eddies coincided with the location of largest radius (∼over 90 km, near 27°S, 43°E). The same is true for the anticyclonic eddies, with exception for those formed around the eastern parts of the domain (∼24°S, 53°E), where the largest anticyclonic eddies (Figure 16b) had smaller amplitudes (∼10 cm, Figure 16d).

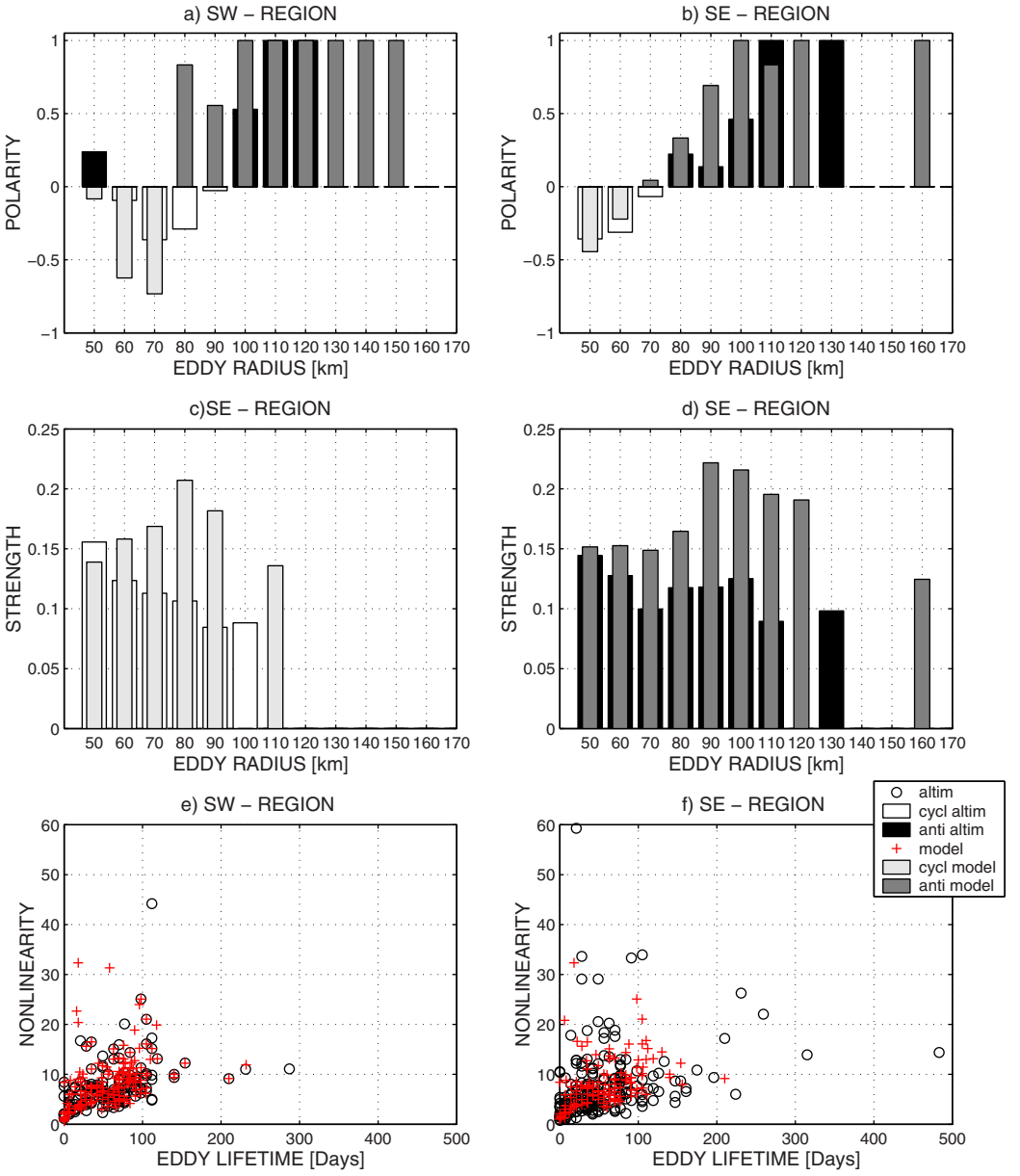

Figure 17. (a and b) eddy polarity, (c and d) eddy strength, and (e and f) nonlinearity. The properties were calculated from both altimetric eddies identified from 14 October 1992 to 31 March 2010, and model eddies (7 years), with a life-time $\tau \geq 60$ days. Except for nonlinearity parameter, eddies of all ages are considered. SE region: 45.10°E–51.10°E, and 32°S–23°S. SW region: 39°E–45°E, and 32°S–23°S. For altimetry: polarization toward cyclones (white bars) and anticyclones (black bars). For the model: polarization toward cyclones (light-gray) and anticyclones (drak-gray). Nonlinearity for altimetry (model) is represented by circles (crosses).

The averaged eddy amplitude for both cyclones (Figure 16c) and anticyclones (Figure 16d) shows that eddies with large mean amplitudes cooccur with the large radii. As remarked by *Chelton et al*. [2011b], these characteristics are consistent with theoretical expectations for large nonlinear eddies proposed by *Rhines* [1979]. From north to south, to the east of about 48°E, the cyclones have a significant lower amplitude than to the west of 48°E (Figure 16c). The same is true for the anticyclones to the east of about 50°E (Figure 16d).

The time period over which an eddy was tracked in the domain with respect to their site of origin was computed and mapped, as presented by *Souza et al*. [2011]. Eddy life-expectancy was defined as the difference between the date when the eddy makes its first appearance and the date since it was last seen [*Halo*, 2012; *Halo et al*., 2014]. It is presented in Figure 16e for cyclones, and in Figure 16f for anticyclones. The dominant time scale both for cyclonic and anticyclonic eddies was ∼120 days. The longest time scale, appeared to be

associated with eddies that formed to the southeast of the Madagascar Basin, between ~32°S and 27°S, and 48°E and 53°E.

Eddy life-time is shown in Figures 16e and 16f. Eddies formed in the eastern parts of the domain have a longer life-expectancy. In the western parts, a significant eddy-shelf and eddy-eddy interactions are known to occur [*de Ruijter et al*., 2004], these may enhance their weakening and dissipation. This result indicates that the eddy amplitude is not the sole factor that determines the longevity of an eddy, as has been inferred by *Chelton et al*. [2011b]. Cyclonic eddies (Figure 16e) generated near the Madagascar coast have a longer life-expectancy than the anticyclones (Figure 16f).

To determine the dominant eddy type in the SW and SE of Madagascar, and infer their potential role on the marine connectivity between Madagascar and Africa, relevant dynamical eddy properties are discussed below.

6.4.7. Eddy Polarity, Strength, and Nonlinearity From Altimetry and Model

Figures 17a and 17b show the eddy polarity for the SW and SE regions, respectively, as function of their radii, clustered into 10 km intervals, based on altimetry observations and model output. For altimetry cyclones are represented by white bars and anticyclones by black bars. For the model, cyclones are light-gray bars and anticyclones by dark-gray bars. Eddy polarity provides useful information about the length-scale at which cyclonic eddies are prevalent over anticyclonic eddies [*Chelton et al*., 2011b]. Following *Kurian et al*. [2011], eddy polarity was defined as $(Na-Nc)/(Na+Nc)$, where *Na* and *Nc* are the total numbers of anticyclonic and cyclonic eddies, respectively.

From altimetry product in the SW region, there were eight bands of polarization (Figure 17a). The eddies were polarized toward the cyclones between 60 and 90 km radii, accounting for 50% of the all observed bands. Prevalence of anticyclones occurred at 50 km, and between 100 and 120 km radii, accounting for the other 50%. This result arguably could indicate that a dipolar coherent mesoscale structure is favored to occur in the SW region. Prevalence of cyclonic eddies occurs at smaller-scales, and anticyclonic eddies at larger-scales, except at 50 km. For the SE region (Figure 17b), there were also eight bands of polarization. Prevalence toward cyclones occurred at radii between 50 and 70 km, accounting for 37.5% of all observed bands. The polarization toward anticyclones ranged from 80 to 130 km, accounting for 62.5%. This indicates a tendency for anticyclones at large-scale to dominate over the cyclones in the SE region.

In order to infer the tendency for dominance of large anticyclones over the cyclones, we have inspected the strength of the eddies formed within this region. Here following *Kurian et al*. [2011] and *Liang et al*. [2012], eddy strength was defined as the ratio between the absolute relative vorticity averaged within the eddy, normalized by the planetary vorticity $|\zeta/f|$. Figures 17c and 17d show their distribution as function of cyclonic and anticyclonic radii. Cyclonic eddies were stronger than the anticyclonic at smaller-scale ($R \leq$ 70 km), while the opposite was observed at larger-scales.

From the model product in the SW region (Figure 17a), there were 11 bands of polarization. Cyclones polarization ranged from 50 to 70 km radii, while anticyclones were from 80 to 150 km. In the SE region (Figure 17b), cyclones were between 50 and 60 km, and anticyclones span from 70 to 160 km. In general, the model shows a strong preference for anticyclonic formation at both intermediate (70–80 km) and larger ($\geq$80 km) horizontal scales, while cyclones at smaller-scales. Inspection of their strength in the SE region has shown a tendency for cyclones to reach their maximum strength at 80 km (Figure 17c) and anticyclones at 90 km radii (Figure 17d). The asymmetry between cyclones and anticyclones has been observed in in situ measurements, laboratory experiments, as well as in numerical model solutions [*McWilliams*, 1985; *Graves et al*., 2006; *Perret et al*., 2006, 2011]. However, theoretical explanations for this asymmetry remain an ongoing study, suggesting different controlling mechanisms [*Cushman-Roisin and Tang*, 1990; *Willett et al*., 2006; *Graves et al*., 2006; *Perret et al*., 2006, 2011]. Because the eddies in our study are not wind forced, rather they form through current instabilities, interpretations linked to the wind activity are not considered here. The eddies in the SE region are mostly formed through barotropic instabilities of the SEMC in the upper ocean, and baroclinic instabilities at intermediate depths (Figure 11). Possible explanation for the observed asymmetry here is made through inspections of the eddy strength, which measure their robustness. For altimetry, our analysis of the eddy strength in the SE shows a considerable weakening of the cyclones while increasing radii (Figure 17c). Under such weakening regime, the prevalence of the large anticyclones over cyclones could be associated to the tendency for weakening of the

large cyclonic structures, probably induced by the background flow [*Perret et al*., 2011]. Similar process also has been reported in the northeastern tropical Pacific [*Liang et al*., 2012]. However, in the model, such pattern can only be observed for cyclonic eddies with radii larger than 70 km. From 50 to 80 km they increase in strength, then they decrease. It is likely that other processes (not mentioned here) are also playing an important role.

To investigate the ability of the eddies to trap materials, we have inspected the nonlinearity parameter of eddies of all ages in the SW and SE regions, both for altimetry and model output. Following *Chelton et al*. [2007, 2011b], eddy nonlinearity parameter was defined as the ratio between the eddy rotational velocity and their propagation speed (u/c). For $u/c > 1$ implies that the eddies are nonlinear, thus are able to trap material in their core [*Chelton et al*., 2011b; *Kurian et al*., 2011]. Figures 17e and 17f show the distribution of the eddy nonlinearity as function of their life-time, as observed by altimetry (circle-symbols) and model output (cross-symbols). For altimetry product in both regions the eddies were highly nonlinear (by 99.16% in SE and by 100% in SW region). In the SW region the peak of nonlinearity was $\sim$44.2, observed within the eddies with a life-time slightly greater than 100 days (relatively old-age), implying that their evolutionary history may play an important role. Whereas in the SE region the peak was $\sim$59.3, for eddies with a life-time of $\sim$30 days (relatively young-age), implying that their generation history may play an important role. In the SW region cyclonic eddies were the most abundant, had strongest relative vorticity, were most energetic, were longest-lived and traveled longest distances, suggesting that they are most effective structures to trap materials in their core and transport for long distances, evidently from Madagascar toward the African continent. For the model, both in SW and SE region, all eddies were by 100% highly nonlinear, and have shown a general preference to reach their maximum peak at relatively young age $\sim$30 days. Eddies measured in situ in this region by *de Ruijter et al*. [2004] also have shown to carry their water characteristics as they drifted away. Global inspection of mesoscale eddies by *Chelton et al*. [2007] has shown that the vast majority of eddies in the ocean are nonlinear. Especially, so outside the tropical band between 20°N and 20°S, with preferential tendency for cyclones in the southern hemisphere and anticyclones in the northern [*Chelton et al*., 2011b].

7. Conclusion

The region to the south of Madagascar has high levels of mesoscale eddy variability. Based on altimetric observations, two-regions have been characterized with distinctly different mesoscale activity and eddy characteristics. The mesoscale activity in the region to the southeast of Madagascar (SE) is strongly impacted by seasonal variability. In this region, satellite altimetry indicates that the overall impact of the seasonality accounts for $\sim$44% of the maximum kinetic energy, while in the southwest region (SW) it is only slightly affected ($\sim$18%).

Analysis of energy conversion terms in the model output throughout the water column indicates that there is seasonality on eddy formation, both by barotropic and baroclinic instabilities: maximum in winter (JJA) and minimum in summer (DJF). The eddies are mainly formed in the upper ocean (0–300 m) by barotropic instability and at intermediate depths (800–2000 m) by baroclinic instability. Barotropic instability dominates to the southeast of Madagascar and baroclinic instability to the southwest. A significant phase variation was found between the model derived seasonal cycle of the volume transport of the SEMC and barotropic instabilities, indicating that the surface eddy formation is strongly modulated by the seasonal intensification of the background flow. Another important conclusion based in the model is that the eddies have a significant contribution to the large-scale circulation, but not persistent throughout the year, occurring mainly during the fall season (MAM).

The use of an automatic algorithm to identify and track eddies with a reasonable accuracy allowed to access a wider range of eddy properties in altimetry and model data, providing information of their preferential sites of birth, annual occurrence (6–13 per year), eddy mean diameter (124–178 km), mean amplitude (9–28 cm), eddy mean life-time (90–183 days), and maximum traveling distances (325–1052 km). It also allowed to access preferential eddy scales for polarization, being cyclones favored at small-scale, and anticyclones at large-scale.

Both model and observations have shown that nearly all eddies to the south of Madagascar were highly nonlinear and are potential vectors of connectivity between Madagascar and Africa.

Both satellite and model have shown that eddies formed around the south of Madagascar escaped the study area moving toward the Agulhas Current (Figures 14e, 14g, and 14h). Considering that they have lived longer than 9 months, if they reach the Agulhas retroflection region as some studies suggest, then it could be expected an inter-ocean exchange of biological communities between Indian and Atlantic oceans. A study aiming to understand the impact of such connectivity in the ecosystems would be worth to be considered.

Acknowledgments
The authors gratefully acknowledge the funding from the IRD research grant, and the Nansen-Tutu Centre (NTC) for Marine Environmental Research at the Oceanography department, University of Cape Town, supported by the Nansen Scientific Society. The altimetry data set was provided by the SSALTO/DUACS, CNES, AVISO. Special acknowledgment to Johnny Johannessen for hosting me at NERSC (Bergen, Norway) where most of this paper was written.

References

Azevedo, J. L. L., L. R. de Oliveira, J. F. A. de Sousa, I. D. Soares, and M. M. Mata (2008), Os Processos de Conversão de Energías nos Oceanos, uma Revisão do Diagrama de Lorenz, *Rev. Bras. Geophys.*, *26*, 153–172.

Backeberg, B. C., and C. Reason (2010), A connection between the South Equatorial Current north of Madagascar and Mozambique Channel, *Geophys. Res. Lett.*, *37*, L04604, doi:10.1029/2009GL041950.

Biastoch, A., and W. Krauss (1999), The role of mesoscale eddies in the source regions of the Agulhas Current, *J. Phys. Oceanogr.*, *29*, 2303–2317.

Birol, F., and R. Morrow (2001), Sources of the baroclinic waves in the Indian Ocean, *J. Geophys. Res.*, *106*, 9145–9160.

Birol, F., and R. Morrow (2003), Separation of quasi-semiannual Rossby waves from the eastern boundary of the Indian Ocean, *J. Mar. Res.*, *61*, 707–723, doi:10.1357/002224003322981110.

Carpine-Lancre, J., R. Fisher, B. Harper, P. Hunter, M. Jones, A. Kerr, A. Laughton, S. Ritchie, D. Scott, and M. Whitmarsh (2003), *The 100-Year Story of the General Bathymetric Chart of the Oceans*, vol. 5, 149 pp., GITC bv, Lammer, Netherlands.

Chapman, P., S. F. DiMarco, R. E. Davis, and A. C. Coward (2003), Flow at intermediate depths around Madagascar based on ALACE float trajectories, *Deep Sea Res., Part II*, *50*, 1957–1986.

Chelton, D. B., R. A. deSzoeke, M. G. Schlax, K. E. Naggar, and N. Siwertz (1998), Geographical variability of the first-baroclinic Rossby radius of deformation, *J. Phys. Oceanogr.*, *28*, 433–460.

Chelton, D. B., M. G. Schlax, R. M. Samelson, and R. A. Szoeke (2007), Global observations of large oceanic eddies, *Geophys. Res. Lett.*, *34*, L15606, doi:10.1029/2007GL030812.

Chelton, D. B., P. Gaube, M. G. Schlax, J. J. Early, and R. M. Samelson (2011a), The influence of nonlinear mesoscale eddies on near surface oceanic chlorophyll, *Science*, *334*, 328–332, doi:10.1126/science.1208897.

Chelton, D. B., M. G. Schlax, and R. M. Samelson (2011b), Global observations of nonlinear mesoscale eddies, *Prog. Oceanogr.*, *91*, 167–216, doi:10.1016/j.pocean.2011.01.002.

Colas, F., J. C. McWilliams, X. Capet, and J. Kurian (2012), Heat balance and eddies in the Peru-Chile current system, *Clim. Dyn.*, *39*, 509–529, doi:10.1007/s00382-011-1170-6.

Conkright, M. E., R. A. Locarnini, H. E. Garcia, T. D. O'Brien, T. P. Boyer, C. Stephens, and J. I. Antonov (2002), World Ocean Atlas 2001: Objective analyses, data statistics, and figures, CD-ROM documentation, Tech. Rep. 17, Natl. Oceanogr. Data Center, Silver Spring, Md.

Cronin, M., and D. R. Watts (1996), Eddy-mean flow interaction in the gulf stream at 68°W. Part 1: Eddy energetics, *J. Phys. Oceanogr.*, *26*, 2107–2131.

Cushman-Roisin, B. (1994), *Introduction to Geophysical Fluid Dynamics*, 320 pp., Prentice Hall, New York.

Cushman-Roisin, B., and B. Tang (1990), Geostrophic turbulence and emergence of eddies beyond the radius of deformation, *J. Phys. Oceanogr.*, *20*, 97–113.

Cushman-Roisin, B., and J.-M. Beckers (2009), *Introduction to Geophysical Fluid Dynamics: Physical and Numerical Aspects*, 777 pp., Academic, Thayer Sch. of Eng. Dartmouth College, Hanover, N. H.

da Silva, A. M., C. C. Young, and S. Levitus (1994), Atlas of surface marine data 1994, vol. 1: Algorithms and procedures, NOAA Atlas NESDIS 6, U.S. Dep. of Commer., NOAA, Printing Office, Washington, D. C.

de Ruijter, W. P. M., H. Ridderinkhof, J. R. E. Lutjeharms, M. W. Schouten, and C. Veth (2002), Observations of the flow in the Mozambique Channel, *Geophys. Res. Lett.*, *29*(10), doi:10.1029/2001GL013714.

de Ruijter, W. P. M., H. M. van Aken, E. J. Beier, J. R. E. Lutjeharms, R. P. Matano, and M. W. Schouten (2004), Eddies and dipoles around South Madagascar: Formation, pathways and large-scale impact, *Deep Sea Res., Part I*, *51*, 383–400, doi:10.1016/j.dsr.2003.10.011.

de Ruijter, W. P. M., H. Ridderinkhof, and M. W. Schouten (2005), Variability of the southwest Indian Ocean, *Philos. Trans. R. Soc. A*, *363*, 63–76.

Donohue, K. A., and J. M. Toole (2003), A near synoptic survey of the SouthWest Indian Ocean, *Deep Sea Res., Part II*, *50*, 1893–1931.

Donohue, K. A., E. Firing, and L. Beal (2000), Comparison of three velocity sections of the Agulhas Current and Agulhas Undercurrent, *J. Geophys. Res.*, *105*, 585–593.

Ducet, N., P. Y. Le Traon, and G. Reverdin (2000), Global high-resolution mapping of ocean circulation from TOPEX/Poseidon and ERS-1 and -2, *J. Geophys. Res.*, *105*, 19,477–19,498.

Erasmi, W., G. Siedler, and R. Onken (1998), Energy conversion in the Cape Verde Frontal Zone, *J. Geophys. Res.*, *103*, 21,469–21,479.

Everett, J. D., M. E. Baird, P. R. Oke, and I. M. Suthers (2012), An avenue of eddies: Quantifying the biophysical properties of mesoscale eddies in the Tasman Sea, *Geophys. Res. Lett.*, *39*, L16608, doi:10.1029/2012GL053091.

Graves, L. P., J. C. McWilliams, and M. T. Montgomery (2006), Vortex evolution due to straining: A mechanism for dominance of interior anticyclones, *Geophys. Astrophys. Fluid Dyn.*, *100*(3), 151–183.

Gründlingh, M. L. (1985), Features of the circulation in the Mozambique Basin in 1981, *J. Mar. Res.*, *43*, 779–792.

Gründlingh, M. L. (1995), Tracking eddies in the southeast Atlantic and southwest Indian Oceans with TOPEX-POSEIDON, *J. Geophys. Res.*, *100*, 24,977–24,986.

Halo, I. (2012), The Mozambique Channel eddies: Characteristics and mechanisms of formation, PhD thesis, Univ. of Cape Town, Cape Town.

Halo, I., B. Backeberg, P. Penven, I. Ansorge, C. Reason, and J. E. Ullgren (2014), Eddy properties in the Mozambique Channel: A comparison between observations and two numerical ocean circulation models, *Deep Sea Res., Part II*, *100*, 38–53, doi:10.1016/j.dsr2.2013.10.015.

Hansen, D. V., and P. Poulain (1996), Quality control and interpolation of WOCE/TOGA drifter data, *J. Atmos. Oceanic Technol.*, *13*, 900–909.

Isern-Fontanet, J., E. Garcia-Ladona, and J. Font (2006), Vortices of the Mediterranean Sea: An altimetric perspective, *J. Phys. Oceanogr.*, *36*, 87–103.

Jackett, D. R., and T. J. McDougall (1995), Minimal adjustment of hydrostatic profiles to achieve static stability, *J. Atmos. Oceanic Technol.*, *12*, 381–389.
Krakstad, J. O., S. Mehl, R. Roman, J. Escobar-Porras, J. Stapley, B. Flynn, M. Olsen, and I. M. Beck (2008), East Madagascar Current ecosystem survey, Tech. Rep. ASCLME/FAO cruise-1, Inst. of Mar. Res., Bergen, Norway.
Kundu, P. K. (1990), *Fluid Mechanics*, vol. 1, 638 pp., Academic, San Diego, Calif.
Kurian, J., F. Colas, X. Capet, J. C. McWilliams, and D. B. Chelton (2011), Eddy properties in the California Current System, *J. Geophys. Res.*, *116*, C08027, doi:10.1029/2010JC006895.
Lamont, T., M. J. Roberts, R. G. Barlow, T. Morris, and M. A. vander Berg (2010), Circulation patterns in the Delagoa Bight, Mozambique, and the influence of deep ocean eddies, *Afr. J. Mar. Sci.*, *32*, 553–562.
Lathuilière, C., M. Levy, and V. Echevin (2011), Impact of eddy-driven vertical fluxes on phytoplankton abundance in the euphotic layer, *J. Plankton Res.*, *33*, 827–831, doi:10.1093/plankt/fbq131.
Liang, J., J. C. McWilliams, J. Kurian, F. Colas, P. Wang, and Y. Uchiyama (2012), Mesoscale variability in the northern tropical Pacific: Forcing mechanisms and eddy properties, *J. Geophys. Res.*, *117*, C07003, doi:10.1029/2012JC008008.
Lumpkin, R., and M. Pazos (2007), Measuring surface currents with surface velocity program drifters: The instrument, its data and some recent results, in *Lagrangian Analysis and Prediction of Coastal and Ocean Dynamics*, chap. 2, 487 pp., Cambridge Univ. Press, Cambridge, U. K.
Lumpkin, R., and P. J. Flament (2013), Extent and energetics of the Hawaiian lee countercurrent, *Oceanogr. Soc.*, *26*, 58–65.
Lutjeharms, J. R. E. (1988), On the role of the East Madagascar Current as a source of the Agulhas Current, *S. Afr. J. Sci.*, *84*, 236–238.
Lutjeharms, J. R. E. (2006), *The Agulhas Current*, vol. 1, 329 pp., Springer, Berlin.
Lutjeharms, J. R. E., and A. J. da Silva (1988), The Delagoa Bight eddy, *Deep Sea Res., Part A*, *35*, 619–634.
Lutjeharms, J. R. E., and H. R. Roberts (1988), The Natal Pulse: An extreme transient on the Agulhas Current, *J. Geophys. Res.*, *93*, 631–645.
Lutjeharms, J. R. E., and E. Machu (2000), An upwelling cell inshore of the East Madagascar Current, *Deep Sea Res., Part I*, *47*, 2405–2411.
Lutjeharms, J. R. E., and I. Ansorge (2001), The Agulhas Return Current, *J. Mar. Syst.*, *30*, 115–138.
Lutjeharms, J. R. E., N. D. Bang, and C. P. Duncan (1981), Characteristics of the currents east and south of Madagascar, *Deep Sea Res., Part A*, *28*, 879–899.
Lutjeharms, J. R. E., P. M. Wedepohl, and J. M. Meeuwis (2000), On the surface drift of the East Madagascar and the Mozambique Currents, *S. Afr. J. Sci.*, *96*, 141–147.
Marchesiello, P., J. C. McWilliams, and A. Shchepetkin (2003), Equilibrium structure and dynamics of the California Current System, *J. Phys. Oceanogr.*, *33*, 753–783.
Matano, R. P., C. G. Simionato, and P. T. Strub (1999), Modeling the wind-driven variability of the South Indian Ocean, *J. Phys. Oceanogr.*, *29*, 217–230.
Matano, R. P., E. J. Beier, P. T. Strub, and R. Tokmakian (2002), Large-scale forcing of the Agulhas variability: The seasonal cycle, *J. Phys. Oceanogr.*, *32*, 1228–1241.
McGillicuddy, J. D., et al. (2007), Eddy/wind interaction stimulate extraordinary mid-ocean plankton blooms, *Science*, *316*, 1021–1026.
McWilliams, J. C. (1985), Submesoscale, coherent vortices in the ocean, *Rev. Geophys.*, *23*, 165–182.
McWilliams, J. C., and G. R. Flierl (1979), On evolution of isolated non-linear vortices, *Dyn. Atmos. Oceans*, *5*, 43–66.
Morrow, R., F. Birol, D. Griffin, and J. Sudre (2004), Divergent pathways of cyclonic and anticyclonic eddies, *Geophys. Res. Lett.*, *31*, L24311, doi:10.1029/2004GL020974.
Nauw, J. J., H. M. van Aken, J. R. E. Lutjeharms, and W. P. M. D. Ruijter (2006), Intrathermocline eddies in the Southern Indian Ocean, *J. Geophys. Res.*, *111*, C03006, doi:10.1029/2005JC002917.
Nauw, J. J., H. M. van Aken, A. Webb, J. R. E. Lutjeharms, and W. P. M. D. Ruijter (2008), Observations of the southern East Madagascar Current and Undercurrent and Countercurrent system, *J. Geophys. Res.*, *113*, C08006, doi:10.1029/2007JC004639.
Niiler, P. P., A. Sybrandy, K. Bi, P. Poulain, and D. Bitterman (1995), Measurements of the water-following capability of Holey-sock and TRISTAR drifters, *Deep Sea Res., Part I*, *42*, 1951–1964.
Okubo, W. (1970), Horizontal dispersion of floatable particles in the vicinity of velocity singularities such as convergencies, *Deep Sea Res. Oceanogr. Abstr.*, *17*, 445–454.
Omta, A. W., J. Llido, V. Garcon, S. A. L. M. Kooijman, and H. A. Dijkstra (2009), The interpretation of satellite chlorophyll observations: The case of the Mozambique Channel, *Deep Sea Res., Part I*, *56*, 974–988, doi:10.1016/j.dsr.2009.01.011.
Palastanga, V., P. J. van Leeuwen, M. W. Schouten, and W. P. M. D. Ruijter (2007), Flow structure and variability in the subtropical Indian Ocean: Instability of the South Indian Ocean Countercurrent, *J. Geophys. Res.*, *112*, C01001, doi:10.1029/2005JC003395.
Penven, P., V. Échevin, J. Pasapera, F. Colas, and J. Tam (2005), Average circulation, seasonal cycle and mesoscale dynamics of the Peru Current System: A modeling approach, *J. Geophys. Res.*, *110*, C10021, doi:10.1029/2005JC002945.
Penven, P., I. Halo, S. Pous, and L. Marié (2014), Cyclogeostrophic balance in the Mozambique Channel, *J. Geophys. Res. Oceans*, *119*, 1054–1067, doi:10.1002/2013JC009528.
Perret, G., A. Stegner, and M. Farge (2006), Cyclonic-anticyclonic asymmetry of large-scale wakes in the laboratory, *Phys. Fluids*, *18*, 036603.
Perret, G., T. Dubos, and A. Stegner (2011), How large-scale and cyclogeostrophic barotropic instabilities favor the formation of anticyclonic vortices in the ocean, *J. Phys. Oceanogr.*, *41*, 303–328, doi:10.1175/2010JPO4362.1.
Provenzale, A. (1999), Transport by coherent barotropic vortices, *Annu. Rev. Fluid Mech.*, *31*, 55–93.
Quartly, G. D., and M. A. Srokosz (2002), SST observations of the Agulhas and East Madagascar retroflections by TRMM microwave imager, *J. Phys. Oceanogr.*, *32*, 1585–1592.
Quartly, G. D., and M. A. Srokosz (2004), Eddies in the southern Mozambique Channel, *Deep Sea Res., Part II*, *51*, 69–83, doi:10.1098/rsta.2002.1108.
Quartly, G. D., J. J. H. Buck, M. A. Srokosz, and A. C. Coward (2006), Eddies around Madagascar—The Retroflection re-considered, *J. Mar. Syst.*, *63*, 115–129, doi:10.1016/j.jmarsys.2006.06.001.
Rhines, P. B. (1979), Geostrophic turbulence, *Annu. Rev. Fluid Mech.*, *11*, 401–441.
Ridderinkhof, H., and W. P. M. de Ruijter (2003), Moored current observations in the Mozambique Channel, *Deep Sea Res., Part II*, *50*, 1933–1955, doi:10.1016/S0967-0645(03)00041-9.
Ridderinkhof, W., D. Le Bars, A. S. von der Heydt, and W. P. M. de Ruijter (2013), Dipoles of the South-east Madagascar Current, *Geophys. Res. Lett.*, *40*, 558–562, doi:10.1002/GRL.50157.
Rio, M. H., S. Guinehut, and G. Larnicol (2011), The new CNES-CLS09 global mean dynamic topography computed from the combination of GRACE data, altimetry and in-situ measurements, *J. Geophys. Res.*, *116*, C07018, doi:10.1029/2010JC006505.

Robinson, A. R. (1983), *Eddies in Marine Science*, 644 pp., Springer, Berlin.
Roshin, P. R., N. P. Benny, and D. Pushpadas (2010), Oceanic and atmospheric influences on the variability of phytoplankton bloom in the Southwestern Indian Ocean, *J. Mar. Syst.*, *82*, 217–229, doi:10.1016/j.jmarsys.2010.05.009.
Schott, F. A., and J. P. McCreary (2001), The Monsoon circulation of the Indian Ocean, *Prog. Oceanogr.*, *51*, 1–123.
Schott, F. A., M. Fieux, J. Kindle, J. Swallow, and R. Zantopp (1988), The boundary currents east and north of Madagascar. 2: Direct measurements and model comparisons, *J. Geophys. Res.*, *93*, 4963–4974.
Schouten, M. W., W. P. M. de Ruijter, and P. J. van Leeuwen (2002a), Upstream control of Agulhas ring shedding, *J. Geophys. Res.*, *107*(C8), 3109, doi:10.1029/2001JC000804.
Schouten, M. W., W. P. M. de Ruijter, P. J. van Leeuwen, and H. A. Dijkstra (2002b), An oceanic teleconnection between the equatorial and southern Indian Ocean, *Geophys. Res. Lett.*, *29*(16), 1812, doi:10.1029/2001GL014542.
Schouten, M. W., W. P. M. de Ruijter, P. J. van Leeuwen, and H. Ridderinkhof (2003), Eddies and variability in the Mozambique Channel, *Deep Sea Res., Part II*, *50*, 1987–2003, doi:10.1016/S0967-0645(03)00042-0.
Shchepetkin, A. F., and J. C. McWilliams (2005), The regional oceanic modeling system (ROMS): A split-explicit, free-surface, topography-following-coordinate oceanic model, *Ocean Modell.*, *9*, 347–404, doi:10.1016/j.ocemod.2004.08.002.
Siedler, G., M. Rouault, and J. R. E. Lutjeharms (2006), Structures and origin of the subtropical South Indian Ocean, *Geophys. Res. Lett.*, *33*, L24609, doi:10.1029/2006GL027399.
Siedler, G., M. Rouault, A. Biastoch, B. Backeberg, C. J. C. Reason, and J. R. E. Lutjeharms (2009), Modes of the southern extension of the East Madagascar Current, *J. Geophys. Res.*, *114*, C01005, doi:10.1029/2008JC004921.
Souza, J. M. A. C., C. de Boyer Montegut, and P. Y. Le Traon (2011), Comparison between three implementations of automatic identification algorithms for the qualification and characterization of mesoscale eddies in the South Atlantic Ocean, *Ocean Sci.*, *7*, 317–334, doi:10.5194/os-7-317-2011.
Srokosz, M. A., and G. D. Quartly (2013), The Madagascar Bloom: A serendipitous study, *J. Geophys. Res. Oceans*, *118*, 14–25, doi:10.1029/2012JC008339.
Stramma, L., and J. R. E. Lutjeharms (1997), The flow field of the subtropical gyre in the South Indian Ocean into the Southeast Atlantic Ocean: A case study, *J. Geophys. Res.*, *99*, 14,053–14,070.
Ternon, J.-F., M. J. Roberts, T. Morris, L. Hancke, and B. Backeberg (2014), In situ measured current structures of the eddy field in the Mozambique Channel, *Deep Sea Res., Part II*, *100*, 10–26, doi:10.1016/j.dsr2.2013.10.013.
Tew-Kai, E., and F. Marsac (2009), Patterns of variability of sea surface chlorophyll in the Mozambique Channel: A quantitative approach, *J. Mar. Syst.*, *77*, 77–88, doi:10.1016/j.jmarsys.2008.11.007.
Thorpe, S. A. (2007), *An Introduction to Ocean Turbulence*, vol. 1, 240 pp., Cambridge Univ. Press, Cambridge, U. K.
Tomczak, M., and J. S. Godfrey (1994), Regional oceanography: An introduction, *Bull. Am. Meteorol. Soc.*, *2*, 390.
Tsugawa, M., and H. Hasumi (2010), Generation and growth mechanism of the natal pulse, *J. Phys. Oceanogr.*, *40*, 1597–1612.
van Leeuwen, P. J., W. P. M. de Ruijter, and J. R. E. Lutjeharms (2000), Natal Pulses and the formation of Agulhas rings, *J. Geophys. Res.*, *105*, 6425–6436.
Weiss, J. (1991), The dynamics of enstrophy transfer in two-dimensional hydrodynamics, *Physica D*, *48*, 273–294.
Willett, C. S., R. R. Leben, and M. F. Lavin (2006), Eddies and tropical instability waves in the eastern tropical Pacific: A review, *Prog. Oceanogr.*, *69*, 218–238.
Zhai, X., H. L. Johnson, and D. P. Marshall (2010), Significant sink of ocean-eddy energy near western boundaries, *Nat. Geosci.*, *3*, 607–612, doi:10.1038/NGEO943.